Coastal Engineering 205 (2026) 104946

Contents lists available at ScienceDirect

Coastal Engineering

journal homepage: www.elsevier.com/locate/coastaleng

A local phase-shift approach for predicting wave-group-forced infragravity waves under directional seas

Ad Reniers [a,*], Gal Akrish [a,b], Marcel Zijlema [a]

[a] Department of Hydraulic Engineering, Delft University of Technology, Delft, The Netherlands
[b] School of Mechanical Engineering, Tel Aviv University, Israel

ARTICLE INFO

Keywords:
Infragravity waves
Phase shift
SWAN surfBeat
Coast3D field validation

ABSTRACT

Accurate prediction of Wave-Group-Forced (WGF) InfraGravity (IG) waves depends on resolving the corresponding phase shift, typically achieved through a coupled phase – amplitude equation. However, this approach requires a grid resolution that resolves the structure of the wave groups making it computationally expensive at regional scales.

To address this limitation, an existing local expression for the phase shift of normally incident WGF-IG waves has been extended to account for directional seas. The extended formulation is verified against predictions from the coupled phase – amplitude model using bichromatic wave forcing over a uniformly sloping beach for a wide range of sea-swell conditions. Results show that the local approach performs well in the off-resonant region for obliquely incident waves. When applied outside this regime, however, its accuracy decreases, with performance varying depending on sea-swell and bathymetric conditions.

The coupled and local phase shift approaches are also validated with observations obtained during the Coast3D field experiment. The total, incoming and outgoing IG waves are predicted with comparable skill and root mean square error for both methods. The good match using the local expression is attributed to the fact that the conditions during Coast3D correspond to directionally broad sea-swell spectra with relative short peak periods propagating over moderately sloping bathymetry for which the verification showed significant skill. Additional validation with field observations at other locations are necessary to firmly determine the limitations of the use of a local phase shift.

1. Introduction

InfraGravity (IG) waves induced by the groupiness of the sea-swell waves with frequencies less than 0.04 Hz play an important role in runup (Raubenheimer and Guza, 1996), overtopping (Lashley et al., 2022), beach and dune erosion (Roelvink et al., 2009), seiching in harbors (Okihiro et al., 1993), ship motions (Rijnsdorp et al., 2022) and ice fracturing (Bromirski et al., 2010). For a comprehensive overview refer to Bertin et al. (2018). IG waves generated at one coast can arrive at distant shores propagating over oceanic scales (Ardhuin et al., 2014). In coastal seas, where water depths are limited this can lead to a significant increase in the incident IG waves at the coast (Rijnsdorp et al., 2021; Matsuba et al., 2024; Akrish et al., 2025), unlike beaches with shelf breaks where the IG waves are predominantly locally trapped (Smit et al., 2018; Fiedler et al., 2019; Lange et al., 2002). There are many modeling approaches available to predict IG waves in the nearshore zone including (semi-)analytical models (Schäffer, 1993; Zhang et al., 2020; Contardo et al., 2021; Liao et al., 2021, 2023), non-hydrostatic models (Rijnsdorp et al., 2015; Ma et al., 2014; Roeber and Bricker, 2015; Smit et al., 2014), wave-group resolving time domain models (Van Dongeren et al., 2003; Reniers et al., 2006; Olabarrieta et al., 2023; Reyns et al., 2023) and meta models (Pearson et al., 2017). Large scale model applications to predict free IG wave conditions are less ubiquitous but have been performed over global (Ardhuin et al., 2014) and regional scales (Rijnsdorp et al., 2021), using a spectral approach. Recently, Leijnse et al. (2024) introduced a reduced stationary model to predict the incident IG wave height covering 450 km of coastline along the Outer Banks in North Carolina. Here we adopt the spectral approach using SWAN SurfBeat (SB) to predict Wave-Group-Forced (WGF) IG waves (Reniers and Zijlema, 2022).

To predict the WGF-IG response at larger scales it is important that the SWAN-SB wave model can operate at a coarse resolution in the deeper parts ($h > 10$ m). Currently the model uses a coupled IG amplitude and phase-shift equation to predict the evolution of the IG response in a directional wave field assuming mild variations in the

* Corresponding author.
E-mail address: a.j.h.m.reniers@tudelft.nl (A. Reniers).

https://doi.org/10.1016/j.coastaleng.2025.104946
Received 2 August 2025; Received in revised form 29 December 2025; Accepted 30 December 2025
Available online 8 January 2026

cross-shore profile at a near alongshore uniform coasts. The phase-shift is defined as the phase difference between the wave group and forced IG wave away from 180°. However, these coupled equations require a grid spacing that resolves the structure of the wave groups, $\Delta x = O(10)m$, making it computationally expensive at regional scales. This in turn inhibits the practical use of the coupled model approach on large scales. To overcome this problem the use of a local expression of the phase shift that is independent of the IG amplitude is explored.

Janssen et al. (2003) provide a local physics-based formulation of the WGF-IG phase shift. This formulation includes the effects associated with small cross-shore changes in depth for a normally incident bichromatic wave train forcing an IG wave. To be able to use this local expression in the presence of a frequency-directional sea-swell spectrum, the formulation is generalized to the case of obliquely incident bichromatic waves on an alongshore uniform beach. This generalized formulation has been verified with more accurate predictions using the coupled model for the phase shift and WGF-IG amplitude using oblique bichromatic wave forcing over a constantly sloping beach for a wide range of sea-swell wave conditions. Next, it has been validated for conditions representative for the nearshore area by comparing with observations of the incident IG conditions during the Coast3D field experiment (Soulsby, 1999; Ruessink et al., 2001; van Rijn et al., 2003).

2. Methods

In the following, the cross-shore evolution of the WGF-IG waves over a planar beach is described with the Infragravity Energy Model (IEM) (Reniers and Zijlema, 2022). The IEM is used to (inter-) compare predictions of the IG response using the fully coupled evolution equation and the generalized local expression to calculate the phase shift. The first test considers a series of bichromatic forcing conditions over a planar beach with varying bed slopes, wave frequencies and directions. Here, the wave-group forcing is obtained from the Infragravity Amplitude Model (IAM) (see Appendix A for a short description). The second test uses the wave-group forcing from SWAN-SB for a frequency-directional sea-swell spectrum (see Appendix B) to compute the WGF-IG response and compare with field observations of the incident, reflected, and total IG wave heights observed during the Coast 3D (C3D) field experiment (Soulsby, 1999).

2.1. Infragravity Energy Model (IEM)

The WGF-IG wave energy balance is given by eq. 15 of (Reniers and Zijlema, 2022):

$$\frac{\mathrm{d}c_g \cos\theta_f h\hat{U}_f^2}{\mathrm{d}x} = -\left(\Delta k_x \hat{U}_{f,x}\hat{F}_{xx} + \Delta k_y \hat{U}_{f,y}\hat{F}_{xy}\right)\sin\psi_c - \hat{U}_{f,x}\frac{\mathrm{d}\hat{F}_{xx}}{\mathrm{d}x}\cos\psi_c \tag{1}$$

where c_g is the group velocity, θ_f the incidence angle, h is the water depth, $\hat{U}_f$ the WGF-IG velocity amplitude, with $\hat{U}_{f,x} = \hat{U}_f\cos\theta_f$, $\hat{U}_{f,y} = \hat{U}_f\sin\theta_f$, and ψ_c the phase shift. Δk_x and Δk_y are the cross-shore, x, and alongshore, y, component of the WGF-IG wave number Δk:

$$\Delta k_x = \Delta k\cos\theta_f \tag{2}$$

$$\Delta k_y = \Delta k\sin\theta_f$$

The corresponding wave-group forcing is given by:

$$\tilde{F} = F_{xx} + \frac{2\Delta k_y}{\Delta k_x}F_{xy} + \frac{\Delta k_y^2}{\Delta k_x^2}F_{yy} \tag{3}$$

with:

$$F_{xx} = -\frac{\hat{S}_{xx}}{\rho}\left(1-Q_b\right), F_{xy} = -\frac{\hat{S}_{xy}}{\rho}\left(1-Q_b\right), F_{yy} = -\frac{\hat{S}_{yy}}{\rho}\left(1-Q_b\right) \tag{4}$$

where $\hat{S}_{ij}$ correspond to the radiation stress modulation amplitudes and Q_b is the fraction of breaking waves. Given the bichromatic wave group forcing and concurrent phase shift the WGF-IG energy can be computed with a finite difference equation (see Reniers and Zijlema (2022) for details).

2.2. Coupled phase-shift evolution equation for bichromatic waves

The coupled evolution equation for the phase shift, ψ_c, between an obliquely incident bichromatic wave group and the corresponding IG response on an alongshore uniform mildly sloping beach is given by (see Appendix C for details):

$$\frac{\mathrm{d}\psi_c}{\mathrm{d}x} = -\frac{\mu\Delta k_x}{2} + \frac{\Delta k_x}{2gh\hat{\eta}_f}|\tilde{F}|\cos(\psi_c) + \frac{1}{gh\hat{\eta}_f} \times \left(\frac{\mathrm{d}F_{xx}}{\mathrm{d}x} + \frac{F_{xx}}{2\Delta k_x}\frac{\mathrm{d}\Delta k_x}{\mathrm{d}x} + \frac{\Delta k_y}{\Delta k_x}\frac{\mathrm{d}F_{xy}}{\mathrm{d}x}\right)\sin(\psi_c) \tag{5}$$

with g as the gravitational acceleration and the generalized resonance mismatch given by:

$$\mu = \frac{1}{\cos^2(\theta_f)}\left(1 - \frac{c_g^2}{gh}\right) \tag{6}$$

This is a directional modification of the resonance mismatch obtained by Janssen et al. (2003) for normally incident WGF-IG waves, resulting in an increased mismatch for obliquely incident IG waves. The WGF-IG wave amplitude is given by:

$$\hat{\eta}_f = \hat{U}_f\frac{h}{c_g} \tag{7}$$

thereby coupling the WGF-IG amplitude, $\hat{\eta}_f$ to the phase shift ψ_c.

2.3. Generalized local phase shift formulation for obliquely incident bichromatic waves

Janssen et al. (2003) provide a local formulation of the WGF-IG phase shift for the off-resonant region, i.e. $\mu = O(1)$, including the effects associated with small changes in depth in the case of a normally incident bichromatic wave train forcing an IG wave. Including the directional properties of the sea-swell waves making up the bichromatic wave train, a more general phase shift formulation is obtained (see Appendix D):

$$\psi_l = \frac{1}{\mu\Delta k_x}\left(\frac{2}{\tilde{F}}\frac{\mathrm{d}\tilde{F}}{\mathrm{d}x} - \frac{1}{h}\frac{\mathrm{d}h}{\mathrm{d}x} - \frac{2}{\mu}\frac{\mathrm{d}\mu}{\mathrm{d}x} + \frac{1}{\Delta k_x}\frac{\mathrm{d}\Delta k_x}{\mathrm{d}x} - \frac{2\mu}{\tilde{F}}\frac{\mathrm{d}F_{xx}}{\mathrm{d}x} - \frac{\mu}{\tilde{F}}\frac{F_{xx}}{\Delta k_x}\frac{\mathrm{d}\Delta k_x}{\mathrm{d}x} - \frac{2\mu}{\tilde{F}}\frac{\Delta k_y}{\Delta k_x}\frac{\mathrm{d}F_{xy}}{\mathrm{d}x}\right) \tag{8}$$

which is independent of the WGF-IG amplitude, but does include the effects of mild spatial variations in the cross-shore bathymetry as expressed by the terms on the right hand side of Eq. (8). These terms include the changes in WGF forcing, water depth, resonance mismatch and shoaling (terms 1–4) as well as a number of interaction terms (5–7). In the local approach, the coupled phase shift ψ_c in Eq. (1) is replaced with local phase shift ψ_l, Eq. (8), to predict the evolution of WGF-IG wave amplitude and subsequently compared to the coupled model results.

2.4. WGF-IG boundary condition

In the case of a horizontal bed and stationary forcing, it is assumed that the equilibrium solution corresponds to a constant $\psi_c = 0$. In that case, Eq. (5) reduces to:

$$\hat{\eta}_f = \frac{|\tilde{F}|}{gh\mu} \tag{9}$$

In the case of a sloping bed the phase shift is not expected to be equal to zero. To that end, a local correction is applied by including an estimate of the expected change in the phase shift:

$$\frac{\mathrm{d}\psi_c}{\mathrm{d}x}|_{x=0} \simeq \frac{\psi_{l,1} - \psi_{l,0}}{\Delta x} = \frac{\Delta\psi_l}{\Delta x}|_{x=0} \tag{10}$$

by evaluating Eq. (8) at the first two points of the grid at the offshore boundary, denoted by the subscripts 0 and 1 respectively. To obtain the

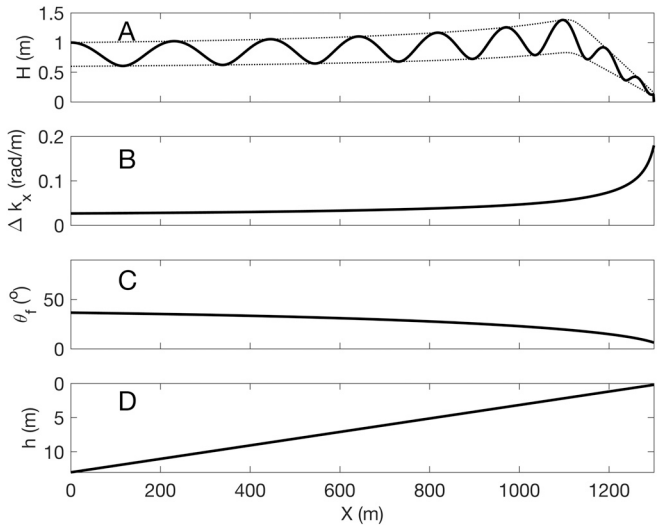

Fig. 1. IAM prediction of the wave-group transformation for an obliquely incident bichromatic wave train with two primary wave components with frequencies of 0.08 Hz and 0.12 Hz respectively. The first component has a wave amplitude of 0.4 m and the second of 0.1 m. The first component is normally incident and the second is obliquely incident at an angle of 15° at the offshore boundary. Panel A: Snapshot of wave-group varying wave height H (solid line) and corresponding envelope (dashed line). Panel B: Cross-shore wave-group number Δk_x. Panel C: Wave forcing angle θ_f by the obliquely incident wave groups. Panel D: Corresponding water depth h.

corresponding WGF-IG amplitude the left hand side of Eq. (5) is then set to Eq. (10) and with $\psi_c = \psi_{l,0}$:

$$\hat{\eta}_f = \frac{\Delta k_x |\tilde{F}| \cos(\psi_{l,0}) + 2\left(\frac{\mathrm{d}F_{xx}}{\mathrm{d}x} + \frac{F_{xx}}{2\Delta k_x}\frac{\mathrm{d}\Delta k_x}{\mathrm{d}x} + \frac{\Delta k_y}{\Delta k_x}\frac{\mathrm{d}F_{xy}}{\mathrm{d}x}\right)\sin(\psi_{l,0})}{2gh\left(\frac{\Delta\psi_l}{\Delta x}|_{x=0} + \frac{\mu\Delta k_x}{2}\right)} \tag{11}$$

2.5. Bichromatic wave-group forcing from IAM

The wave-group transformation for a bed slope of 1:100 computed with the IAM shows the modulated wave height H (see panel A of Fig. 1) for a bichromatic wave field made up of two primary waves of 0.4 m and 0.1 m amplitude with corresponding frequencies of 0.08 Hz and 0.12 Hz, and offshore directions of 0° and 15° degrees respectively. Shoaling is apparent up to $x = 1100$ m, after which wave breaking occurs, resulting in a decay of the wave height and associated modulation. The wave-group length decreases with decreasing water depth resulting in an increase in the cross-shore wave-group number (see panels B and D). As the two primary waves refract towards the coast the incidence angle for the WGF-IG wave is decreasing accordingly (see panel C). The output of the wave group transformation, obtained with the IEM (see Appendix A and Reniers and Zijlema (2022) for details), yields the radiation stresses used to calculate the cross-shore evolution of the WGF-IG wave. This will be done for the range in forcing conditions given in Appendix E Table E.1.

2.6. Coast3D field experiment

To validate the local phase shift expression, observations of infragravity wave conditions obtained during the Coast3D (C3D) field experiment will be used (Soulsby, 1999; Ruessink, 1999). This experiment was executed in Egmond aan Zee situated along the North Holland coast in the Netherlands during the fall of 1998. The bathymetry displays an outer bar located around $X = -500$ m and an inner bar around $X = -200$ m with some minor alongshore variability (see top panel in Fig. 2). The offshore depth is approximately 13 m with respect

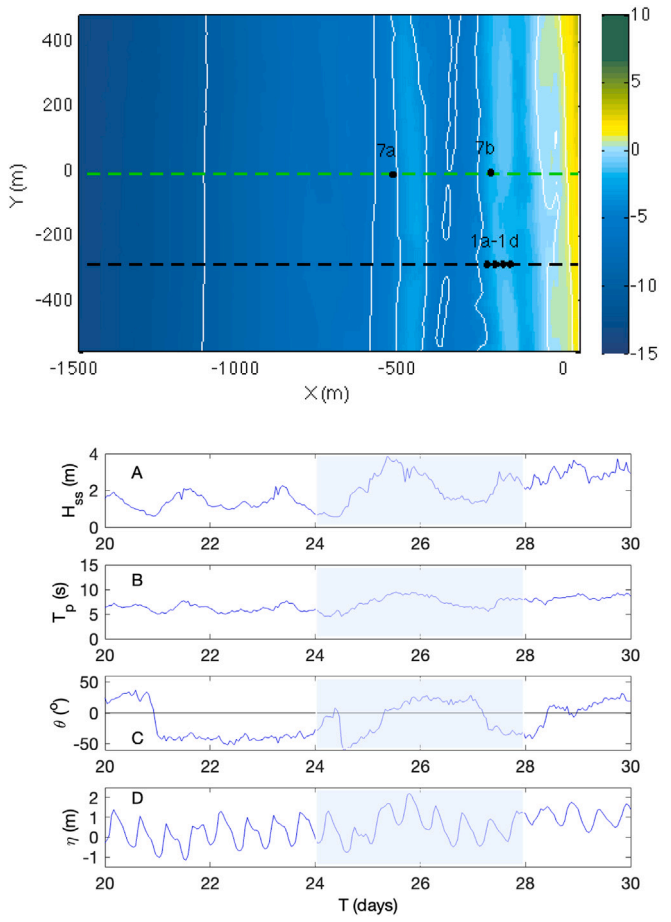

Fig. 2. Upper panel: Bathymetry during the Coast3D field experiment with water depth referenced to mean sea level in (m) indicated by the colorbar. The bathymetry has been rotated to align the x-axis with the local shore normal. Instrument positions are indicated by the black dots. 7a and 7b correspond to stand-alone pressure sensors and 1a–1d to combined pressure and velocity (puv) meters. The main and secondary transects are indicated by the black and green dashed lines respectively. Lower panels: Observed hydrodynamic conditions at the offshore wave buoy. Panel A. Root mean square sea-swell wave height. Panel B: Peak period. Panel C: Mean nautical wave direction with respect to the shore normal. Panel D: Tide and surge elevation. Period used for validation indicated by the shaded area from 24–28 October 1998.

to mean sea level (MSL). Sea-swell wave conditions were measured with a directional wave buoy located at 15 m depth approximately 5 km south of the field site. The period from October 24–28 is used for the model validation (see panels A-D in Fig. 2). During this time, both mild and storm conditions are present with a maximum root mean square wave height for the incident sea-swell waves of 4 m. The peak periods range between 5 s and 10 s with wave incidence angles varying around the shore normal. During the storm conditions on the 25th and 26th the tidal modulation is elevated by the wind-driven surge.

There are two transects that will be used in the comparison aligning with the stand-alone pressure sensors and the puv sensors respectively (see upper panel in Fig. 2). At the locations of the puv sensors the Maximum Entropy Method (MEM, Lygre and Krogstad (1986)) is used calculate the frequency-directional surface elevation spectrum, $E(f,\theta)$, of the infragravity waves with frequencies between 0.01 Hz and 0.04 Hz using linear wave theory to translate pressure to surface elevation. This method ignores the presence of bound IG waves and may result in directional errors if the bound waves are dominant (Matsuba et al., 2022). Furthermore, there is no separation of the locally generated Free IG (FIG) waves and those that originate from distant

coasts (Rijnsdorp et al., 2021; Akrish et al., 2025), thus potentially resulting in an under prediction of the incident IG waves by the WGF-IG model. Integrating over the onshore directed IG waves, the incident IG wave heights are obtained which are compared with the predictions:

$$H_{ig,i} = 2\sqrt{2\int_{0.01\ \mathrm{Hz}}^{0.04\ \mathrm{Hz}}\int_{\theta=-90^o}^{\theta=+90^o} E(f,\theta)d\theta df} = 2\sqrt{2m_0} \tag{12}$$

The corresponding mean direction of the incident IG waves is obtained from the first-order moment:

$$D_{ig,i} = \tan^{-1}\left(\frac{\int_{0.01\ \mathrm{Hz}}^{0.04\ \mathrm{Hz}}\int_{\theta=-90^o}^{\theta=+90^o}\sin(\theta)E(f,\theta)d\theta df}{\int_{0.01\ \mathrm{Hz}}^{0.04\ \mathrm{Hz}}\int_{\theta=-90^o}^{\theta=+90^o}\cos(\theta)E(f,\theta)d\theta df}\right) \tag{13}$$

and similarly for the incident IG wave period:

$$T_{ig,i} = \frac{\int_{0.01\ \mathrm{Hz}}^{0.04\ \mathrm{Hz}}\int_{\theta=-90^o}^{\theta=+90^o} f^{-1}E(f,\theta)d\theta df}{m_0} \tag{14}$$

Equivalent expressions for $H_{ig,o}$, $D_{ig,o}$ and $T_{ig,o}$ are used to calculate the characteristics of the outgoing IG waves by integrating over the outgoing directions only ($-180° < \theta < -90°$ and $90° < \theta < 180°$). For the stand-alone pressure sensors, 7a–7b, directional information is not available and the IG parameters are calculated from the surface elevation frequency spectrum:

$$H_{ig,t} = 2\sqrt{2\int_{0.01\ \mathrm{Hz}}^{0.04\ \mathrm{Hz}} E(f)df} \tag{15}$$

The sea-swell wave heights are obtained at all instrument locations from the surface elevation spectrum (thus including potential reflections):

$$H_{ss} = 2\sqrt{2\int_{0.04\ \mathrm{Hz}}^{0.3\ \mathrm{Hz}} E(f)df} \tag{16}$$

where linear wave theory is used to translate the pressure spectrum to a surface elevation spectrum. These observations will be used to compare with the predicted sea-swell wave transformation.

2.7. SWAN-SB model setup for Coast3D experiment

The model domain for the SWAN-SB computations is extended in the alongshore direction to avoid wave shadow effects. To that end, the bathymetry (see top panel in Fig. 2) is copied at both lateral sides to create a locally alongshore uniform extension of 500 m each. The cross-shore and alongshore grid spacing are 10 m and 40 m respectively.

The offshore model boundary conditions are obtained from a directional wave buoy providing significant sea-swell wave height, peak period and mean wave direction (see panels A–C in Fig. 2). These wave parameters are used to prescribe the offshore frequency-directional sea-swell spectrum using a Jonswap shape and a $\cos^m(\theta - \theta_m)$ directional distribution with m set to 2 corresponding to directional spreading of $O(30°)$ consistent with observations.

The directional resolution is set to 10° to represent a 360° directional distribution and properly resolve the directional spreading. A logarithmic frequency distribution is used to represent the sea-swell conditions ranging between 0.04 Hz and 0.3 Hz. For the WGF-IG calculations the frequency range is from 0.01 Hz to 0.04 Hz with a constant 0.01 Hz interval. The incident WGF-IG boundary condition is given by Eq. (11). The model is run in stationary mode at 3-hour intervals. The combined tide and surge level is prescribed as a spatially constant change in water depth. The reflection point is defined at a water depth of 0.1 m near the shoreline with a frequency-dependent reflection coefficient for the incident IG wave energy (van Dongeren et al., 2007; Battjes and Janssen, 1978):

$$R = 0.2\pi\beta_H^2 \tag{17}$$

with the beta parameter given by:

$$\beta_H = \frac{m_s}{\omega_{ig}}\sqrt{\frac{g}{H_{ig,in}}} \tag{18}$$

using a beach slope m_s of 1:40 based on the measured bathymetry at the upper beach face and an incident IG wave height of $O(0.25)$ m as representative conditions based on observations during the experiment and ω_{ig} as the radian IG frequency.

The model output consists of frequency-directional spectra for the sea-swell and IG waves throughout the model domain. These spectra are substituted in Eqs. (12)–(16) to derive the corresponding model predictions for the wave height, direction and wave periods at the instrument locations. The comparisons with the observations will be performed for the phase shift obtained with both the coupled model and the local expression. The wave energy dissipation by depth-limited wave breaking is computed with the breaker model of Battjes and Janssen (1978) using a constant $\gamma = 0.65$ to define the maximum wave height used in their dissipation formulation. In addition to breaking the current SWAN-SB model simulations include shoaling and refraction. Effects of quadruplets, wind, bed friction, currents and wave setup have been excluded.

2.8. Error metrics

To evaluate the phase shift expression three error metrics are considered. The root mean square error is given by:

$$\epsilon(G) = \sqrt{\overline{(G_p - G_o)^2}} \tag{19}$$

where the subscript p refers to the predictions and o to the observations of variable G. The overbar indicates averaging over all relevant observations. The bias between predictions and observations is given by:

$$b(G) = \overline{G_p - G_o} \tag{20}$$

The corresponding scatter index is given by:

$$SCI(G) = \frac{\epsilon(G)}{max(\sigma(G_o), \bar{G}_o)} \tag{21}$$

with σ as the standard deviation and the overbar to represent the mean where a SCI of 0 corresponds to perfect model skill.

3. Results

3.1. Verification with bichromatic wave-group forcing

Using the wave conditions corresponding to test B_{01} (see Table E.1) presented in Fig. 1, the phase shift prediction using the local approach is compared with the more accurate results of the coupled model (see left panel of Fig. 3). The local approximation matches well offshore up to a value of $\mu \simeq 0.5$ (compare the dash-dotted black and green lines in the left panel of Fig. 3) with the dominant contributions given by terms 1–3 shown in the right panel consistent with (Liao et al., 2021). For smaller μ values, the phase shift expression displays a relatively stronger increase followed by a rapid decrease within the surfzone (see panel A in Fig. 1 for the surfzone location) whereas the coupled model estimate gradually levels off. The strong increase is mainly related to the decrease in both water depth and resonance mismatch in the shoaling zone (see terms 2 and 3 in the right panel of Fig. 3). Within the surfzone, the changes in the wave-group forcing outweighs all other terms combined (see term 1 in the right panel of Fig. 3) resulting in a rapid decrease of the phase shift. To verify the local phase shift expression, both the phase shift and WGF-IG wave amplitude are compared with the coupled model predictions through several examples with different bed slope, mean frequency, difference frequency, difference angle and mean wave height (see Table E.1 for an overview).

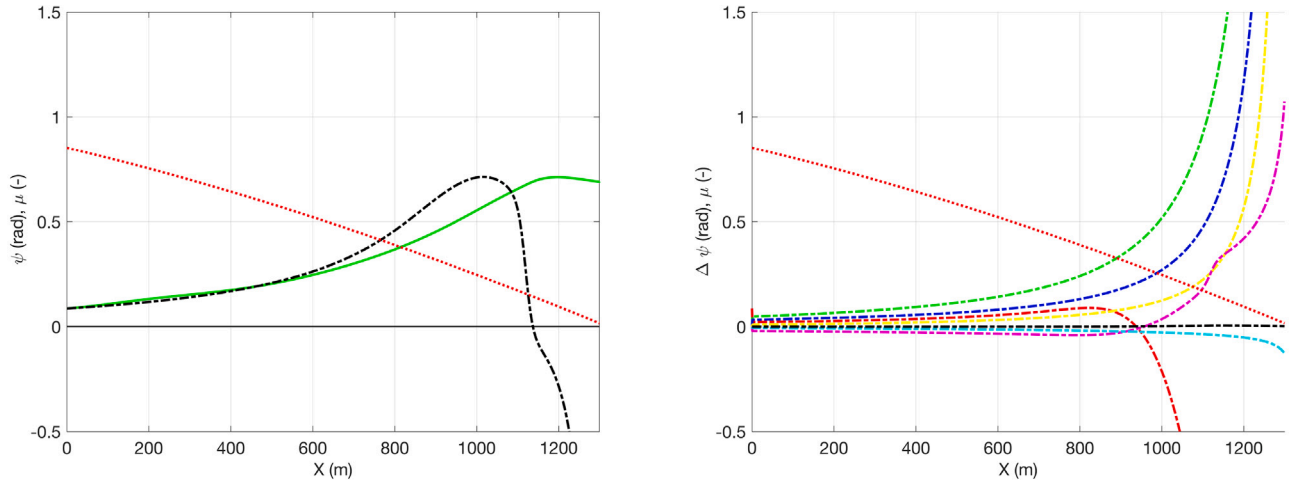

Fig. 3. Left panel: Predictions of the phase shift forced by the conditions shown in Fig. 1 using the coupled (Eq. (5), green line) and the local expression (Eq. (8), black dash-dotted line). Right panel: Individual contributions to the local expression (red, green, blue, yellow, magenta, cyan and black dash-dotted lines corresponding to contributions 1 to 7 of the right-hand-side of Eq. (8)). The resonance mismatch (Eq. (6) red dotted line) is given as a reference.

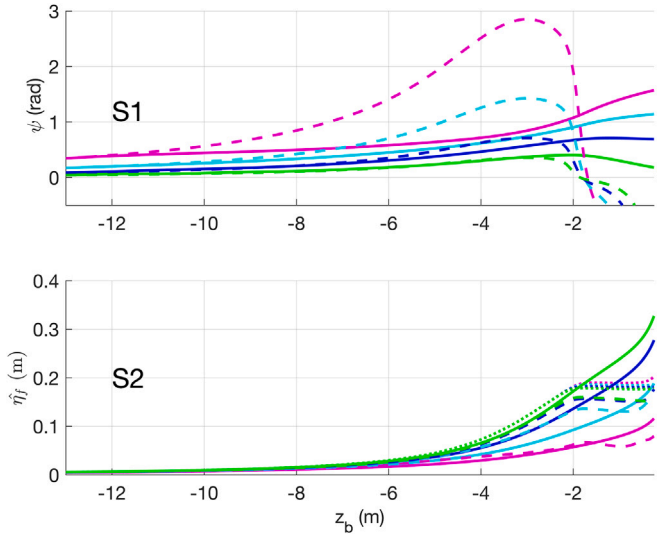

Fig. 4. Phase shift (upper panel) and WGF-IG amplitude (lower panel) predictions for an obliquely incident bichromatic wave train with conditions presented in Fig. 1 using the coupled model, Eq. (5) (solid lines) and the local phase shift, Eq. (8) (dashed lines), as function of bed level, z_b. Corresponding bed slopes are 1:25 (magenta), 1:50 (cyan), 1:100 (blue), 1:200 (green). The corresponding equilibrium solution for the WGF-IG amplitude, Eq. (9), is given by the dotted lines in the lower panel.

3.1.1. Bed slope

Keeping the offshore boundary conditions for the wave-group forcing the same, the bed slope is varied from 1:25 to 1:200 (corresponding to the S-tests given in Table E.1). Given the fact that the wave forcing conditions are similar for a given depth, the equilibrium WGF-IG amplitude is similar for all beach slopes (see panel S2 in Fig. 4). Using the more accurate coupled model shows that the predicted phase shift for the steeper slopes is significantly larger than for the milder slopes (see panel S1 in Fig. 4). Even though the phase shift increases for steeper slopes it is not enough to keep up with the equilibrium WGF-IG amplitude outside the surfzone. Inside the surfzone the mismatch between the equilibrium solution and the actual WGF-IG amplitude determines the behavior of the phase shift. At locations where the WGF-IG amplitude is below the equilibrium solution, the phase shift continues to increase, as happens for slopes of 1:25 and 1:50. When the equilibrium is exceeded, the phase shift reduces as can be observed for the milder slopes of 1:100 and 1:200.

The mismatch of the local phase shift expression with the coupled solution outside the surfzone is largest for steeper slopes (see panel S1 in Fig. 4). For the milder slopes, the local solution matches well up to the surfzone. Inside the surfzone, the local solution deviates strongly compared to the coupled model solution with negative phase shifts where the latter showspositive values.

Using the local phase shift expression the differences in the WGF-IG amplitude outside of the surfzone are relatively small, especially for the milder slopes (see panel S2 in Fig. 4). The fact that the WGF-IG amplitude matches closely for the steepest beach slope in the presence of a large mismatch in the predicted phase shift is treated in the Discussion. Inside the surfzone, the predictions are biased low, consistent with the negative phase shift estimates using the local approach resulting in the highest SCI for the mildest slope (see Test S04 in Table E.1).

3.1.2. Difference frequency

In the following the mean frequency is kept the same, but the difference frequency is varied from 0.01 Hz to 0.04 Hz (see F-tests in Table E.1). The near-similarity in the group velocity implies that the resonance mismatch is similar in all cases. Given the fact that the second of the two primary wave components is obliquely incident, the wave-group forcing angle also varies, with the largest angle for the smallest frequency difference. As a result, the equilibrium solution for the longest WGF-IG wave is the smallest (see panel F2 in Fig. 5) given the dependence of the coupling coefficient on the difference angle between the primary waves, which is weaker for the longer IG waves resulting in smaller growth rates for the latter (Reniers et al., 2002).

For difference frequencies larger than 0.01 Hz, differences between the local and coupled solution are small outside the surfzone (see panel F1 in Fig. 5). The phase shift for the lowest difference frequency of 0.01 Hz is clearly under-predicted. The reverse occurs within the surfzone where the phase shift for the 0.01 Hz difference frequency is well predicted but the others are over-predicted by the local expression. The concurrent prediction for the WGF-IG amplitudes shows a reasonable match using the local approximation (see panel F2 in Fig. 5). Also the absolute difference for the lowest difference frequency of 0.01 Hz is small due to the previously mentioned small growth rate. The results are summarized in Table E.1.

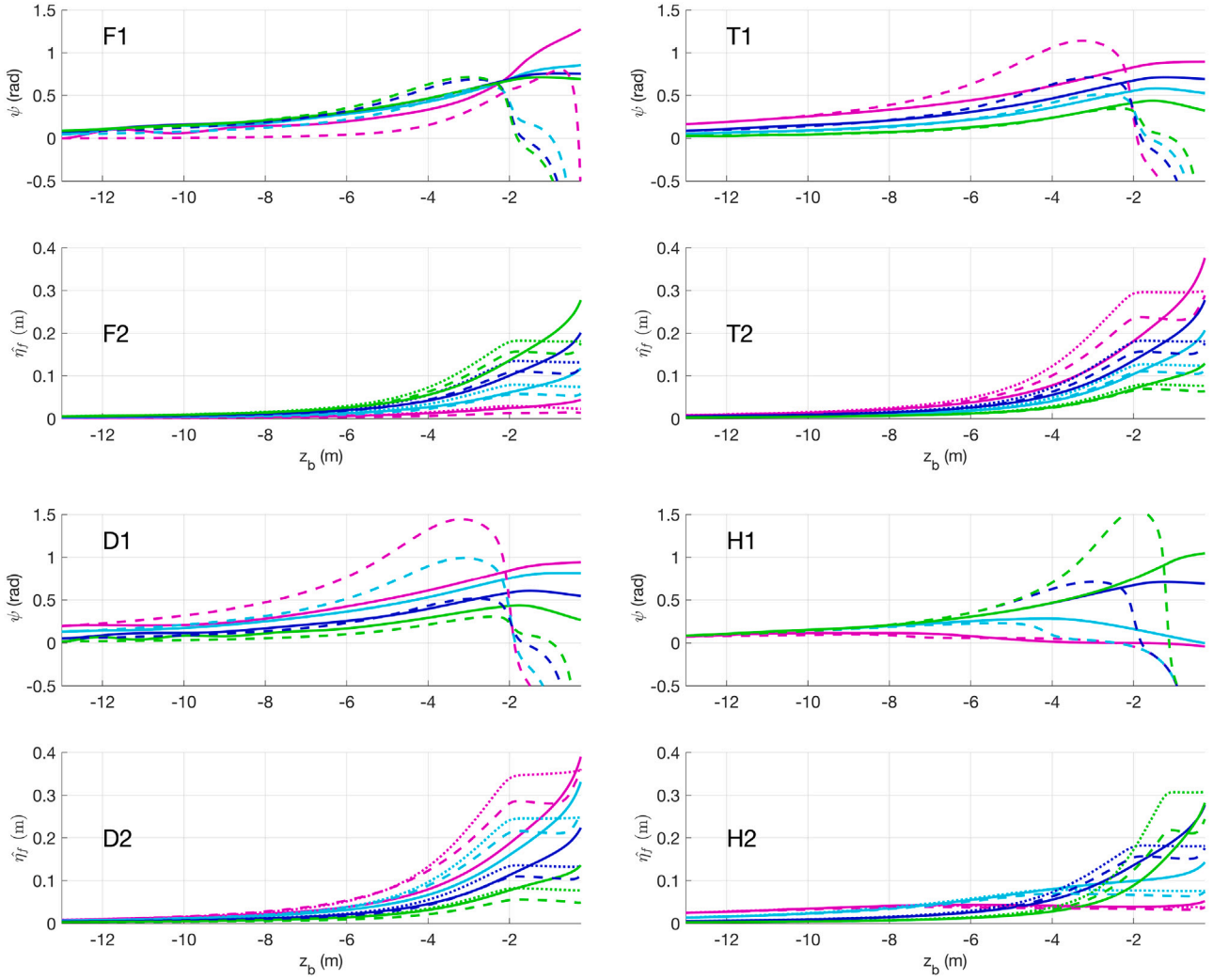

Fig. 5. Comparison of phase shift (panels #1) and IG amplitude (panels #2) predictions using the coupled equation, Eq. (5) (solid lines) and the local expression, Eq. (8) (dashed lines) as function of bed level, z_b. Panels F: Comparison with frequency differences of 0.01 Hz (magenta), 0.02 Hz (cyan), 0.03 Hz (blue), 0.04 Hz (green). Panels T: Comparison with different mean wave periods of 12.5 s (magenta), 10 s (blue), 8.5 s (cyan) and 7 s (green). Panels D: The same comparison with different directions of the second primary wave component of 0° (magenta), 10° (cyan), 20° (blue) and 30° (green). Panels H: Comparison with different first wave component amplitudes of 2.0 m (magenta), 1.0 m (cyan), 0.4 m (blue) and 0.1 m seconds (green). The second component is kept at 0.1 m. The corresponding equilibrium solutions for the WGF-IG amplitude, Eq. (9), are given by the dotted lines in the panels #2.

3.1.3. Mean wave period

Next, the mean wave period is varied from 7 s to 12.5 s but the difference frequency is kept the same (see T-tests in Table E.1 for the forcing conditions). The resonance mismatch is inversely proportional to the mean period and the interaction coefficient. Keeping the difference frequency at 0.04 Hz but increasing the mean wave period thus leads to a strong increase in the equilibrium IG wave height response (see dotted curve in Fig. 5, panel T2) and to earlier near-resonance conditions and thus higher phase shift and corresponding sub-harmonic energy transfer values (as shown by the other curves in Fig. 5, panels T1 and T2). To reach the equilibrium amplitude the growth rate is the largest for the longer waves primary waves (see panel T1 in Fig. 5).

With the local approximation the best results outside the surfzone are obtained for the shorter mean wave periods (see panel T1 in Fig. 5). The largest difference is obtained for the longest mean wave period of 12.5 s, where the phase shift is significantly over predicted. Inside the surfzone, the phase shift is again under-predicted with negative values using the local approximation.

The over prediction of the phase shift for the longer mean wave periods results in a concurrent over prediction of the IG wave amplitude outside the surfzone (see panel T2 in Fig. 5). In contrast, a good match is obtained for the short mean wave periods. Inside the surfzone, the amplitude is under-predicted consistent with the negative values for the phase shift obtained with the local approximation. See the SCI values in Table E.1 for the overall performance.

3.1.4. Difference angle

Keeping the first wave component at 0° the incidence angle of the second primary wave component is varied between 0° and 30° (see Table E.1). An increased difference angle leads to a weaker coupling and the equilibrium solution of the forced WGF-IG wave decreases accordingly (see panel D2 in Fig. 5) exemplifying the role of directional spreading in the IG response. The corresponding growth rate is thus the largest for the normally incident bichromatic wave pair and the smallest for the most oblique pair (see panel D1 of Fig. 5). The largest mismatch using the local approximation is obtained for normal incidence, where the phase shift is significantly overestimated with decreasing depth. This mismatch is reduced with increasing difference angle (see panel D1 in Fig. 5), and a small under prediction is observed for the largest difference angle of 30°. Inside the surfzone, all local phase shift estimates become again negative whereas the coupled solution stays positive. The corresponding amplitude predictions outside

the surfzone are consistent with the over/under predictions using the local approximation (see panel D2 in Fig. 5), with the largest mismatch for the case of normally incident waves (see SCI in Table E.1).

3.1.5. Mean wave height

The wave amplitude of the first primary wave component is varied between 0.1 m and 2 m, while the second component is kept at 0.1 m (see details for H tests in Table E.1) representing very mild to storm conditions. The equilibrium solution for the WGF-IG amplitude is the smallest for the largest mean wave height (see panel H2 in Fig. 5). This is a consequence of the fact that the wave-group modulation is reduced in the presence of breaking (see Eq. (4)), resulting in the smallest forcing for the highest mean wave height within the surfzone. For the mildest conditions the wave-group forcing persists in much shallower depth resulting in a larger equilibrium WGF-IG amplitude. This is reflected in the accompanying phase shift which is very small for the largest mean wave height and has maximum values for the smallest mean wave height.

At the boundary outside the surfzone the phase shift is well predicted using the local expression. Inside the surfzone, the closest match for the phase shift is obtained for the largest mean wave height (see panel H1 in Fig. 5). The phase shift for the smallest mean wave height is significantly over predicted with decreasing depth. This is attributed to the fact that the resonance mismatch, μ, is small at the onset of breaking at very shallow depths.

The WGF-IG amplitude predictions using the local expression track the evolution of the predictions using the more accurate coupled model outside the surfzones (see panel H2 in Fig. 5). Inside the surfzone the match is less favorable, except for the largest mean wave height. Again results are summarized in Table E.1.

3.1.6. Summary of bichromatic wave-group forcing

To evaluate the dependence of the model predictions using the local phase shift on the resonance mismatch μ, the SCI is computed for model output points for which $\mu > \mu_t$, with μ_t as a threshold value. This is done for all individual tests presented in Table E.1. Averaging over all tests shows that there is a significant decrease in the SCI with increasing μ_t consistent with the fact that the largest errors are occurring within the near-resonant regions close to shore. The SCI level off around $\mu_t \simeq 0.5$, delineating the off-resonant region where both have significant model skill with $SCI_{\hat{\eta}}$ and SCI_{ψ} of 0.11 and 0.17 respectively. Although using the local approximation of the phase shift throughout the model domain results in increased errors, the predictions stay bounded and explain a significant part of the WGF-IG amplitude variability with an overall $SCI_{\hat{\eta}}$ of 0.37.

3.2. Validation with Coast3D field experiments

To validate the local approach under real-world conditions, its performance in predicting IG waves is examined using observations from the Coast3D field experiment introduced in Section 2.6. Comparison of all predictions of the incident root mean square sea-swell wave height at the various instrument locations, evaluated at three-hour intervals over the 4-day period, shows good correspondence when using a constant breaker parameter γ. This is reflected by the small bias and SCI (see Table F.1). These results provide confidence in the modeled sea-swell wave transformation and establish a solid basis for assessing the IG wave predictions that follow.

An example of the SWAN-SB output using the coupled model for day 25 at 10 pm shows the wave transformation of the sea-swell waves over the barred profile during storm conditions with an offshore root mean square wave height of $O(3)$ m. Wave breaking causes a gradual decay in wave height offshore followed by more intense wave damping over the outer and inner bar and at the beach (see Fig. 7A). The model predictions and observations compare well in this case. The differences in the predicted wave heights at both transects are very similar, consistent with the assumption of near-alongshore uniformity in the bathymetry. The corresponding frequency-integrated directional IG spectrum has a mean incident IG angle slightly oblique with respect to the shore normal and becomes narrower with decreasing depth (see Fig. 7B). Near the shoreline, the incident IG energy is reflected (see Fig. 7C). The majority of this energy radiates offshore as leaky IG waves combined with local trapping close to the water line and the inner bar. Integrating the directional IG spectrum for the incident and outgoing IG waves shows that the first is generally underestimated at the instrument locations (see Fig. 7D). Consequently, this also holds for the total IG wave height. Again, the differences in the predictions at the two transects are small consistent with the assumption of near alongshore uniformity (compare green and black lines in panel D). Performing the same computations using the local phase shift expression shows the same trends in the predicted IG wave height, accompanied with a modulation at the scales of the underlying sand bars (compare dashed and solid lines in Fig. 7D). This is a result of the instantaneous response of the local phase shift expression to bed-slope variations whereas the coupled model slowly adapts to these changes.

3.2.1. Total IG wave height

Next, the total root mean square IG wave height is compared at the six instrument locations for the duration of the validation period (see Fig. 8). The model skill between the different approaches is comparable, with root mean square errors of $O(5\ \mathrm{cm})$ at all instrument locations compared with the observations. The largest mismatch is observed at instrument 7a (see top panel). The predictions using the coupled model show a persistent negative bias, resulting in a general underestimation of the IG wave height, particularly during the more energetic sea-swell conditions on days 25 and 26 of October. The bias is reduced when using the local expression. The overall performance is summarized in Table F.2.

3.2.2. Incoming and outgoing IG wave height

The primary interest is in the incoming IG waves as these correspond to the boundary conditions for dune erosion impacts (e.g. van Wiechen et al. (2023)) and potential overtopping at dikes (e.g. Lashley et al. (2022)). Adding the refractively trapped IG waves to the incident WGF IG waves (see panels B–D of Fig. 7), the incoming IG wave height can be compared with the observations. Overall, the match with the observations is fair. Using the coupled approach gives a persistent underestimation during storm conditions (see Fig. 9) resulting in a negative bias (see Table F.3). Using the local approximation, this bias is again reduced.

The results for the outgoing IG wave height are comparable for both methods with errors of $O(3\ \mathrm{cm})$ and minimal bias (see Table F.4). This is somewhat surprising given the earlier mentioned negative bias in the incoming IG wave height suggesting that the reflection coefficient, Eq. (17), is on average slightly too high.

3.2.3. Frequency-dependent IG wave height

Next, the incident IG wave height for individual IG frequencies at bin-intervals of 0.01 Hz starting at 0.005 Hz are compared with observations at sensor location 1a (see left panel of Fig. 10). The overall comparison again shows a favorable match using the local phase shift expression or the coupled model. The mismatch is comparable for all frequency bins with the largest errors during storm conditions. The earlier observed negative bias at instrument 1a using the coupled model is present in all frequency bins. This bias is again reduced if the local approximation is used leading to a smaller SCI (see Table F.5).

The predicted outgoing IG wave height for the individual IG frequency bins also match reasonably well with observations (see right panel of Fig. 10). The observations show that the outgoing IG wave height for the higher IG frequencies is significantly smaller than for the lower IG frequencies whereas the incoming IG wave heights are similar (compare left and right panels). Using the frequency-dependent

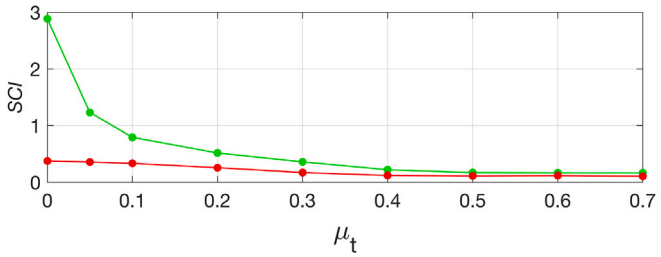

Fig. 6. Test-averaged SCI_{ψ} for the phase lag (green line) and $SCI_{\tilde{\eta}}$ for the WGF-IG amplitude (red line) considering values for which $\mu > \mu_t$ in Eq. (21).

reflection coefficient according to Eq. (17) this behavior is on average well reproduced by the model predictions. The largest mismatch is again observed during the storm conditions on the 25th of October at high tide (see Fig. 2 for the mean water elevation), specifically in the higher IG frequency bins of 0.02 to 0.04 Hz. A summary of the model performance is provided in Table F.6).

3.2.4. Mean IG directions and periods

The integral parameters for the mean IG wave direction and mean period, Eqs. (13) and (14), are compared at location 1a (see Fig. 11). The incident mean IG wave period shows minimal variation in the observations during the validation period, which is well matched by the model predictions, independent of the phase shift approach (see panel A). The mean IG period for the outgoing waves displays more variability, with an improved match obtained using the local expression for the phase shift (see panel B and Table F.7). The mean incident direction for the incoming IG waves is on average underpredicted (see panel C), resulting in a negative bias of $O(10)^o$ independent of the phase shift approaches. For both the overall trend in the directional changes with the progression of the storm on 25 and 26 of October is reproduced. This also holds for the mean direction of the outgoing IG waves (see panel D).

3.2.5. Summary of Coast3D validation

The overall performance of the SWAN-SB model is encouraging for this range of conditions using the coupled phase shift equation or the local expression with root mean square errors of $O(5$ cm) in the predicted total, incoming and outgoing IG wave heights (see Tables F.2–F.4) at the instrument locations. The results obtained using the coupled model are biased low in comparison with the estimates obtained with the local expression.

4. Discussion

In the following we discuss the results with the bichromatic forcing and the validation of SWAN-SB predictions of IG wave heights during the Coast3D field experiment and put the findings in perspective.

4.1. Factors influencing the applicability of the local expression for directional seas

Using the local expression in the bichromatic test cases, the largest mismatch in the phase shift is obtained for the steepest bed slope (panel S1 in Fig. 4). However, given the reduced growth rate for steeper slopes, the mismatch in the WGF-IG amplitude stays limited compared to predictions using the more accurate coupled approach to predict the phase shift (panel S2). This also holds within the surfzone, resulting in a SCI comparable to the other slopes (see test S_{01} in Table E.1).

The beach at the Coast3D field site is characterized by a mild slope offshore followed by multiple sand bars in the surfzone and a steeper beach face. To evaluate the performance of the local phase shift the mismatch with the coupled model is examined for the duration of the

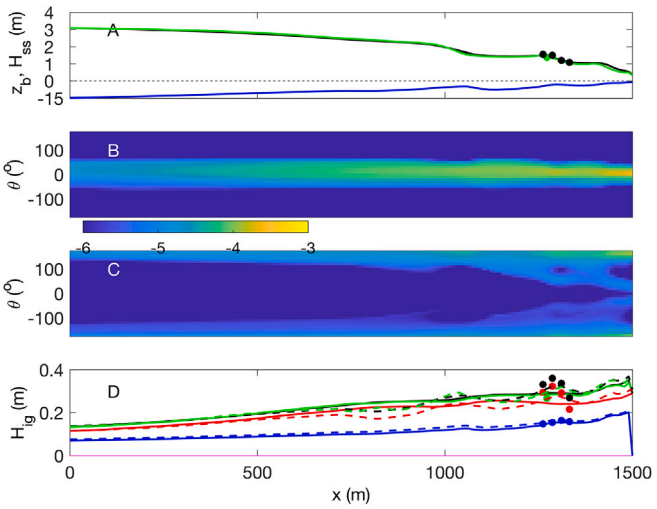

Fig. 7. SWAN-SB predictions for Oct 25 at 10 pm. Panel A: H_{ss} at main (black line) and secondary transect (green line). Bed level given as a reference (blue line with respect to total water level). Observations by pressure sensor 7a (green dot) and puvs (1a–1d, black dots). Panel B: Frequency-integrated incident directional IG spectrum on a log scale along the main transect for the coupled model. Panel C: Frequency-integrated reflected directional spectrum along the main transect for the coupled model. Panel D: $H_{ig,i}$, $H_{ig,o}$ and $H_{ig,t}$ for the coupled model (red, blue and black solid lines) and the local phase shift approach (corresponding colored dashed lines) compared with observations (dots) at puv locations along the main transect. $H_{ig,t}$ for the coupled model (solid green line) and local approach (dashed green line) compared with observations of stand-alone pressure sensors in the secondary transect (green dot) (see Fig. 3 for the corresponding instrument locations.).

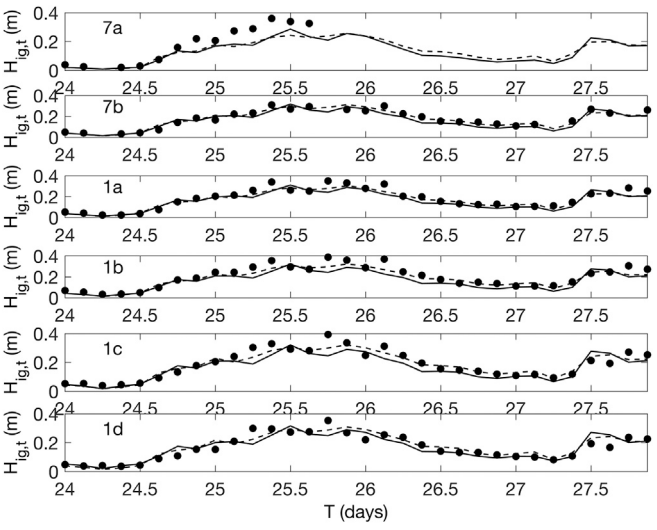

Fig. 8. SWAN-SB predictions for the total root mean square IG wave height during the Coast3D validation period. Model predictions using the coupled (solid lines) and local phase shift (dashed lines) estimates are compared with observations (solid black dots, see Fig. 3 for the corresponding instrument locations).

validation period (see Fig. 12). This shows that the errors are small on the mild offshore slope and the steeper beach face consistent with the verification results. The largest mismatches occur in the vicinity of the breaker bars as the local phase shift reacts instantaneously to the rapid changes in the bed slope and associated wave forcing, whereas the coupled model adapts more slowly (see Fig. 7D). This implies that the error statistics based on the observations are location dependent,

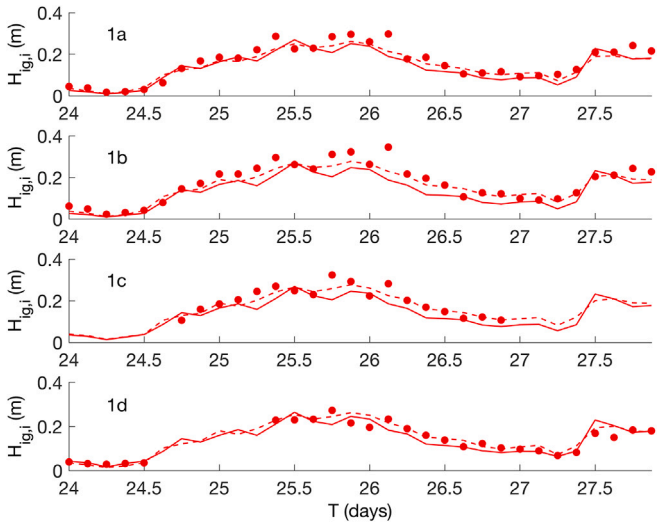

Fig. 9. SWAN-SB predictions for the incoming root mean square IG wave height during the Coast3D validation period. Model predictions using the coupled (solid lines) and local phase shift (dashed lines) estimates are compared with observations (solid red dots, see Fig. 3 for the corresponding instrument locations.).

although the expected error is less than $O(5\ \text{cm})$ (see upper panel of Fig. 12).

For other beaches, more significant errors are anticipated for cases characterized by broad surfzones with very mild slopes, leading to an under estimation of the incoming IG wave height near the water line (see the results for test S04 in panel S2 of Fig. 4). For steeper slopes the prediction errors in the IG wave height are expected to increase significantly as the break point IG generation mechanism is not included (Symonds et al., 1982; Baldock, 2012). And in the presence of steep shoals and sand bars the local errors are likely to increase.

Based on the results for the bichromatic wave forcing using the local expression, the incident IG wave height is over estimated within the shoaling zone when the resonance mismatch, μ, becomes less than O(0.5). The resonance mismatch is smaller for bichromatic waves with a small difference angle and for smaller mean frequencies thus leading to increased errors using the local approach (see D1 and T1 panels in Fig. 5). Therefore, it is expected that directionally narrow-banded long period sea-swell wave forcing will result in significant over-estimation within the shoaling zone compared with the more accurate coupled model approach. However, during Coast3D, swell waves are absent and the locally generated wind sea waves have a relatively broad directional spreading, O(30°), and short mean wave period ($T_p < 8$ s) (see panel B in Fig. 2). The corresponding larger resonance mismatch enables the use of the local expression of the phase shift.

4.2. Possible reasons of the underestimation of WGF-IG wave height by the coupled model

The offshore sea-swell wave conditions during the Coast3D validation period range from small to high, 0.5 m < H_{ss} < 4 m (see Fig. 2). At the beginning of the validation period, on October 24, the incident sea-swell waves are small and the sensors are outside of the surfzone. During this period the IG wave height predictions match well, independent of the phase shift formulation (see Figs. 8–10) consistent with being predominantly located in a off-resonant depth for which the local expression holds (see Fig. 6). During the storm conditions, on 25 and 26 October, the sensors are located in the inner surfzone (see Fig. 7A). For these conditions the WGF-IG amplitude growth is expected to be small (Ruessink, 1998) or even negative where energy from the IG waves is lost to IG-wave breaking (van Dongeren et al., 2007) or transferred back to the sea-swell waves which subsequently dissipate by breaking (De Bakker et al., 2015; Thomson et al., 2006). This recurrence of IG energy, corresponding to a negative phase shift, is not observed in the bichromatic test cases (see magenta line in panel H1 in Fig. 5). Given the fact that this is absent for both approaches, it is unlikely that this is the cause for the observed negative bias in predicting the WGF-IG amplitude during storm conditions when the coupled expression for the phase shift is used (see Fig. 9 and Table F.3). A similar underestimation of the IG wave height for October 25 was obtained by Reyns et al. (2023) using a different model and attributed to the omission of incident free IG waves at the offshore model boundary (Rijnsdorp et al., 2021; Akrish et al., 2025). Furthermore, although the WGF is reduced in the presence of breaking waves, the accompanying change in the phase shift as demonstrated by Schäffer (1993) is not included in either approach. Another limitation is the absence of bar-trapped edge waves in SWAN-SB that are expected to play a role during the experiment (Rijnsdorp et al., 2015). In view of these considerations the more accurate coupled model predictions are expected to exhibit a negative bias. The apparent improved model skill using the local phase shift approach is attributed to the position of the instruments over the inner bar where the WGF-IG wave height is amplified (see Figs. 7D and 12).

4.3. Possible reasons of the underestimation of the IG wave period and direction

Although the mean period of the incident IG waves is well predicted, there is clear under prediction of the corresponding mean incident IG direction (see panels A and C in Fig. 11). This result is independent of the method to calculate the phase shift and could be related to the underestimation of refractively trapped IG waves at this location. The fact that the mean outgoing IG wave direction has a similar bias would support this notion. Whether this refractive trapping is locally ill-predicted as the resonant forcing of edge waves is not present in the model of Reniers and Zijlema (2022) or a result from the arrival of refractively trapped IG waves from adjacent coasts (Rijnsdorp et al., 2021; Matsuba et al., 2024; Akrish et al., 2025) is not clear at the moment.

Somewhat unexpectedly, the mean outgoing IG wave period during storm conditions is best predicted by using the local approximation for the phase shift (see panel B in Fig. 11 and Table F.7). This can most likely be attributed to the improved estimation of the outgoing IG wave height during high surge and tidal levels on October 25 (see results for the 0.02 Hz to 0.04 Hz frequency bins in the right panel of Fig. 10 and corresponding SCI in Table F.6), resulting in a smaller mean outgoing IG period at this time, consistent with the observations. It is noted that for both phase shift approaches an underestimation of the higher IG frequency components is observed during storm conditions. This may be attributed to the reflection estimate, Eq. (17), where a constant beach slope of 1:40 has been used. Generally the beach slope higher up the beach is steeper with increased reflection. As this is only reached during high surge and tide levels this may explain the underestimation. Accounting for the (unknown) time evolution of the beach slope may improve the predictions for the outgoing IG wave height and mean wave period (Okihiro and Guza, 1995; Thomson et al., 2006).

4.4. Summary

The verification shows that the local expression works well, provided the resonance mismatch, μ, is larger than 0.5. Combining the local expression in regions where $\mu > 0.5$ with the more accurate coupled model if $\mu < 0.5$ enables a hybrid approach providing more accurate WGF-IG predictions throughout the model domain. The validation study suggests that this transition point is at the outer edge of the surfzone during storm conditions. This opens up the opportunity to predict the WGF-IG waves in larger domains using coarse grid spacing in off-resonant regions and finer grid spacing in near-resonant regions, provided that the bathymetry is near-uniform in the alongshore.

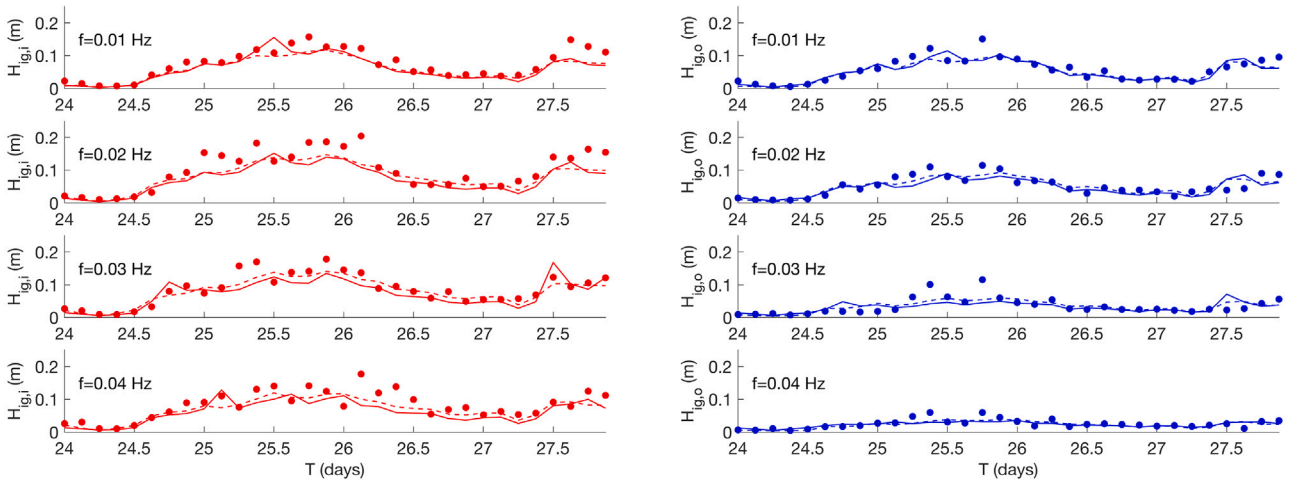

Fig. 10. SWAN-SB predictions for the IG-frequency dependent incoming (left panel) and outgoing (right panel) root mean square IG wave height at sensor location 1a. Model predictions using the coupled (solid lines) and local phase shift (dashed lines) estimates are compared with observations (solid red and blue dots respectively).

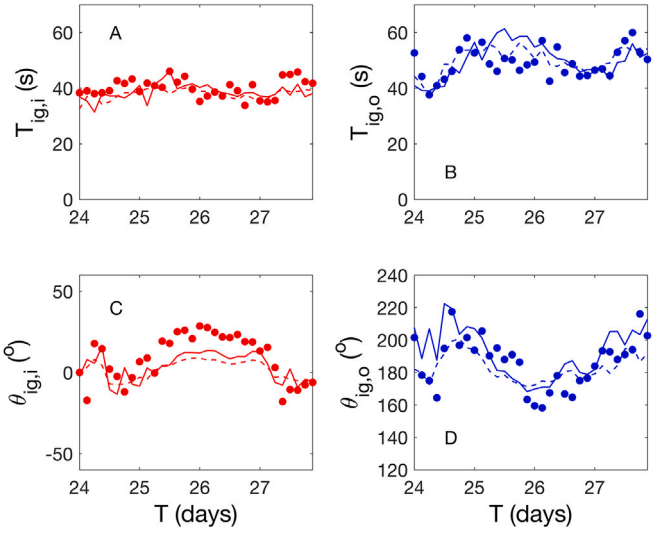

Fig. 11. SWAN-SB predictions for the incoming (panels A and C) and outgoing (panels B and D) mean IG wave period and mean direction at sensor location 1a. Model predictions using the coupled (solid lines) and local phase shift (dashed lines) estimates are compared with observations (solid red and blue dots respectively).

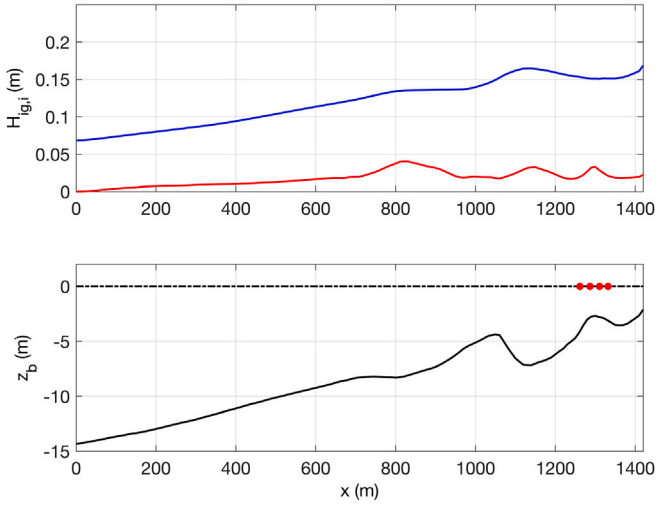

Fig. 12. Upper panel: Predicted incoming root mean square IG wave height for the Coast3D validation period using the coupled model (blue line) and the corresponding root mean square error for the predictions using the local phase shift expression (red line) at the puv transect. Lower panel: Bed elevation (black line) and position of the puv sensors (red dots) given as a reference.

5. Conclusions

A local expression for the phase shift of WGF-IG waves in directional seas has been derived and verified with predictions from a coupled phase–amplitude model using bichromatic wave forcing over a constantly sloping beach for a wide range of sea-swell conditions. The results show that the local phase shift expression performs well in off-resonant regions, particularly for a resonance mismatch $\mu > 0.5$. Applying the local expression uniformly across all conditions reduces accuracy, with performance depending on the sea-swell characteristics (i.e., height, period and spectral spreading), the bed slope, and the associated resonance mismatch (overall scatter index of 0.37 in WGF-IG amplitude).

The coupled and local approaches to estimate the phase shift are validated with observations obtained during the Coast3D field experiment. The results in predicting the total, incoming and outgoing IG waves are comparable in skill and root mean square error for both approaches. This good match is consistent with the insights gained through the bichromatic cases, showing that in the case of directionally broad sea-swell spectra with relative short peak periods propagating over moderately sloping bathymetry, the local phase shift approach should have significant skill, including the shoaling zone and surfzone.

The good match in these two zones is not expected to hold in case of narrow-banded swell or very mild ($m < 0.005$) or very steep bed slopes ($m > 0.04$). Furthermore, the local expression of the phase shift does not account for the fact that changes in the phase shift over a varying bathymetry are not instantaneous and local differences in the presence of steep shoals and sand bars are thus expected.

The apparent underprediction obtained with the coupled phase shift approach is attributed to the omission of edge waves and remotely generated free incident IG waves. As the local approach overpredicts the shoaling rate at the position of the instruments this leads to an erroneously improved match with the observations.

The current work lays the foundation for a hybrid prediction of WGF-IG waves in larger domains by using the local expression at

coarse grid spacing in off-resonant areas and the coupled approach at finer spacing in near-resonant regions. Additional validation with field observations at other locations and different conditions are necessary to determine the validity of the local phase shift approach.

CRediT authorship contribution statement

Ad Reniers: Writing – review & editing, Writing – original draft, Visualization, Validation, Methodology, Funding acquisition, Formal analysis, Conceptualization. **Gal Akrish:** Writing – review & editing, Formal analysis. **Marcel Zijlema:** Writing – review & editing, Software.

Declaration of competing interest

The authors declare that they have no known competing financial interests or personal relationships that could have appeared to influence the work reported in this paper.

Acknowledgments

This research is part of the "Kennis voor Keringen" research for flood defenses program of Rijkswaterstaat, part of the Dutch Ministry of Infrastructure and Water Management. The authors thank Robert Slomp, Robert Vos and Marcel Bottema for supporting this research, and Gerben Ruessink for his help with processing the Coast3D data. The authors also thank Jacco Groeneweg and Joana van Nieuwkoop for their insightful suggestions as well as the reviewers that helped improve this paper.

Appendix A. Wave-group forcing from the infragravity amplitude model

A brief description of the WGF in the IAM is given below for ease of reference. Details can be found in Reniers et al. (2002). The WGF-IG wave equation is given by:

$$gh\frac{\mathrm{d}^2\hat{\eta}}{\mathrm{d}x^2}+g\frac{\mathrm{d}h}{\mathrm{d}x}\frac{\mathrm{d}\hat{\eta}}{\mathrm{d}x}+\Delta\omega^2\hat{\eta}-gh\Delta k_y^2\hat{\eta}= \tag{A.1}$$

$$-\frac{1}{\rho}\left(\frac{\mathrm{d}^2\hat{S}_{xx}\exp\mathrm{i}\int_0^x\Delta k_x dx}{\mathrm{d}x^2}+2\mathrm{i}\Delta k_y\frac{\mathrm{d}\hat{S}_{xy}\exp\mathrm{i}\int_0^x\Delta k_x dx}{\mathrm{d}x}\right.$$

$$\left.-\Delta k_y^2\hat{S}_{yy}\exp\mathrm{i}\int_0^x\Delta k_x dx\right)$$

where x and y are onshore and alongshore directed, h is the local water depth, g the gravitational acceleration, $\hat{\eta}$ is the complex valued total infragravity surface elevation amplitude and $\mathrm{i}=\sqrt{-1}$.

The sea-swell wave group is made up of two incident primary components with amplitudes a_1 and a_2, frequencies ω_1 and ω_2 and directions θ_1 and θ_2 respectively, the corresponding radiation stress amplitudes at the right hand side are given by:

$$\hat{S}_{xx}=\left(\frac{c_g}{c}(1+\cos^2\alpha)-\frac{1}{2}\right)\rho g a_1 a_2 \tag{A.2}$$

and

$$\hat{S}_{xy}=\frac{c_g}{c}(\cos\alpha\sin\alpha)\rho g a_1 a_2 \tag{A.3}$$

and

$$\hat{S}_{yy}=\left(\frac{c_g}{c}(1+\sin^2\alpha)-\frac{1}{2}\right)\rho g a_1 a_2 \tag{A.4}$$

representing the slow modulation of the radiation stresses related to mild changes in depth. The corresponding phase velocity, c and group velocity, c_g, are computed with linear wave theory using the mean frequency of the two components. The bichromatic wave group creates a modulation in the radiation stress with difference frequency $\Delta\omega=\omega_2-\omega_1$, difference cross-shore wave number $\Delta k_x=k_{2,x}-k_{1,x}$ and alongshore wave number $\Delta k_y=k_{2,y}-k_{1,y}$ forcing an infragravity response. The wave direction of the individual sea-swell waves, θ_1 and θ_2, can be computed with Snel's law in case of an alongshore uniform beach, and the difference wave numbers are readily retrieved and the mean sea-swell wave direction. The mean direction α is subsequently obtained from:

$$\alpha=\mathrm{atan}\left(\frac{k_{1,y}+k_{2,y}}{k_{1,x}+k_{2,x}}\right) \tag{A.5}$$

Given the offshore boundary conditions for the two incident waves and a bottom profile the slow cross-shore variation in the radiation stress forcing, $S_{ij}(x)$, is computed with a mean wave energy balance taking into account shoaling, refraction and wave breaking.

Appendix B. Wave-group forcing from SWAN-SB model

The wave-group forcing in SWAN-SB is obtained from the following wave energy balance (Reniers and Zijlema, 2022):

$$\frac{\partial E(\omega,\theta)c_{g,x}}{\partial x}+\frac{\partial E(\omega,\theta)c_{g,y}}{\partial y}+\frac{\partial E(\omega,\theta)c_\theta}{\partial\theta}=-S_{br}(\omega,\theta) \tag{B.1}$$

where E is the energy density, ω the radial frequency and $c_{g,x}$, $c_{g,y}$ and c_θ are the energy density transport velocities in x, y and θ direction respectively. Wave dissipation, S_{br}, is computed with the model of Battjes and Janssen (1978). Here γ acts as a calibration coefficient controlling the maximum sea-swell wave height, $H_{max}=\gamma h$. Given a bathymetry and an offshore sea-swell boundary condition the frequency-directional spectrum, $E(\omega,\theta)$ can be computed Booij et al. (1999). For a specific combination within the frequency-directional spectrum the contribution to the radiation stresses forcing an IG wave can be expressed as:

$$\hat{S}_{xx}(\Delta\omega,\Delta k_y)=\rho g\left(\frac{c_g}{c}(1+\cos^2\alpha)-\frac{1}{2}\right)a_{p,n}a_{q,m} \tag{B.2}$$

and

$$\hat{S}_{xy}(\Delta\omega,\Delta k_y)=\rho g\frac{c_g}{c}(\cos\alpha\sin\alpha)a_{p,n}a_{q,m} \tag{B.3}$$

and

$$\hat{S}_{yy}(\Delta\omega,\Delta k_y)=\rho g\left(\frac{c_g}{c}(1+\sin^2\alpha)-\frac{1}{2}\right)a_{p,n}a_{q,m} \tag{B.4}$$

where the difference frequency is given by $\Delta\omega=\omega_q-\omega_p$ and the difference alongshore wave number is given by $\Delta k_y=k_q\sin(\theta_m)-k_p\sin(\theta_n)$, with p and q referring to the frequency bins and n and m to the directional bins in the offshore frequency-directional sea-swell spectrum. The corresponding amplitudes are obtained from:

$$a_{i,j}=\sqrt{2E(\omega_i,\theta_j)\delta\omega\delta\theta} \tag{B.5}$$

with i and j representing the frequency and directional bins and $\delta\theta$ and $\delta\omega$ corresponding to the directional and frequency resolution of the sea-swell spectrum computed with Eq. (B.1). To expedite the computations the individual primary waves are not traced but scaled with its offshore amplitude.

For a specific pair of incident waves Eq. (1) yields the cross-shore distribution of the WGF velocity, $\hat{U}_f(\Delta\omega,\theta_f)$ and surface elevation $\hat{\eta}_f(\Delta\omega,\theta_f)$. The corresponding WGF surface elevation variance is given by:

$$S_f(\Delta\omega,\theta_f)=\frac{1}{2}\hat{\eta}_f^2(\Delta\omega,\theta_f) \tag{B.6}$$

Solving Eq. (1) for all possible $((p,m),(q,n))$ pairs with $\Delta\omega$ and collecting terms with the same difference frequency and directional bin yields the total WGF-IG surface elevation spectrum:

$$E_f(f,\theta)=\frac{\Sigma S_f(\Delta\omega,\theta_f)}{\delta f\delta\theta} \tag{B.7}$$

with δf as the WGF-IG frequency resolution. The reflection of WGF-IG waves is defined as an outgoing energy flux at the shoreline and computed with Eq. (B.1) ignoring wave breaking resulting in the reflected IG spectrum $E_r(f,\theta)$ that can be combined with $E_f(f,\theta)$ to obtain the full frequency-directional IG spectrum used in Eqs. (12)–(15).

Appendix C. Coupled phase shift equation for obliquely incident bichromatic waves

In the following the coupled phase shift evolution equation for an IG wave forced by a bichromatic wave group at oblique incidence angles is outlined. The starting point is the IG evolution equation A.18 of (Reniers and Zijlema, 2022):

$$-\mu T + \frac{\mathrm{i}}{\Delta k_x}\left(2\frac{\mathrm{d}T}{\mathrm{d}x} + \frac{T}{\Delta k_x}\frac{\mathrm{d}\Delta k_x}{\mathrm{d}x} + \frac{T}{h}\frac{\mathrm{d}h}{\mathrm{d}x}\right) = \tag{C.1}$$

$$-\frac{1}{\rho}\left(-\frac{\hat{S}_{xx}}{gh} - \frac{2\Delta k_y \hat{S}_{xy}}{gh\Delta k_x} - \frac{\Delta k_y^2 \hat{S}_{yy}}{gh\Delta k_x^2} + \frac{\mathrm{i}}{\Delta k_x}\left(\frac{2}{gh}\frac{\mathrm{d}\hat{S}_{xx}}{\mathrm{d}x} + \frac{\hat{S}_{xx}}{gh\Delta k_x}\right.\right.$$
$$\left.\left.\times\ \frac{\mathrm{d}\Delta k_x}{\mathrm{d}x} + \frac{2\Delta k_y}{gh\Delta k_x}\frac{\mathrm{d}\hat{S}_{xy}}{\mathrm{d}x}\right)\right)$$

where T is the cross-shore complex amplitude of the wave-group forced (WGF) IG wave, $\Delta\omega$ the difference frequency and Δk_x and Δk_y the corresponding difference wave numbers in the cross-shore (x) and alongshore (y) direction respectively, h is the water depth, g the gravitational acceleration and $\hat{S}_{ij}$ correspond to the radiation stress components made up by the bichromatic wave. The generalized resonance mismatch μ is given by:

$$\mu = 1 - \frac{\Delta\omega^2 - gh\Delta k_y^2}{gh\Delta k_x^2} \tag{C.2}$$

Using Eq. (2) and $c_g = \Delta\omega/\Delta k$ it can be written as:

$$\mu = \frac{1}{\cos^2(\theta_f)}\left(1 - \frac{c_g^2}{gh}\right) \tag{C.3}$$

Introducing the wave forcing is as:

$$F_{xx} = -\frac{\hat{S}_{xx}}{\rho}, F_{xy} = -\frac{\hat{S}_{xy}}{\rho}, F_{yy} = -\frac{\hat{S}_{yy}}{\rho} \tag{C.4}$$

and multiplying both sides by $\frac{\Delta k_x}{2\mathrm{i}}$ yields:

$$\frac{\mathrm{d}T}{\mathrm{d}x} + \frac{T}{2\Delta k_x}\frac{\mathrm{d}\Delta k_x}{\mathrm{d}x} + \frac{T}{2h}\frac{\mathrm{d}h}{\mathrm{d}x} + \mathrm{i}\frac{T}{2}\mu\Delta k_x = \tag{C.5}$$

$$\frac{\mathrm{i}\Delta k_x}{2gh}\tilde{F} + \frac{1}{gh}\left(\frac{\mathrm{d}F_{xx}}{\mathrm{d}x} + \frac{F_{xx}}{2\Delta k_x}\frac{\mathrm{d}\Delta k_x}{\mathrm{d}x} + \frac{\Delta k_y}{\Delta k_x}\frac{\mathrm{d}F_{xy}}{\mathrm{d}x}\right)$$

where the total wave forcing is given by:

$$\tilde{F} = F_{xx} + \frac{2\Delta k_y}{\Delta k_x}F_{xy} + \frac{\Delta k_y^2}{\Delta k_x^2}F_{yy} \tag{C.6}$$

Following Janssen et al. (2003) this equation is re-written as function of the phase shift, ψ_c:

$$\frac{\mathrm{d}|T|}{\mathrm{d}x} + \mathrm{i}|T|\frac{\mathrm{d}\psi_c}{\mathrm{d}x} + \frac{|T|}{2}\left(\frac{1}{\Delta k_x}\frac{\mathrm{d}\Delta k_x}{\mathrm{d}x} + \frac{1}{h}\frac{\mathrm{d}h}{\mathrm{d}x} + \mathrm{i}\mu\Delta k_x\right) = \tag{C.7}$$

$$\left(\frac{\mathrm{i}\Delta k_x}{2gh}|\tilde{F}| + \frac{1}{gh}\left(\frac{\mathrm{d}F_{xx}}{\mathrm{d}x} + \frac{F_{xx}}{2\Delta k_x}\frac{\mathrm{d}\Delta k_x}{\mathrm{d}x} + \frac{\Delta k_y}{\Delta k_x}\frac{\mathrm{d}F_{xy}}{\mathrm{d}x}\right)\right)\exp(\mathrm{i}\psi_c)$$

Collecting the imaginary contributions the evolution equation for the phase shift is obtained:

$$\mathrm{i}|T|\frac{\mathrm{d}\psi_c}{\mathrm{d}x} + \mathrm{i}\frac{|T|}{2}\mu\Delta k_x = \tag{C.8}$$

$$\frac{\mathrm{i}\Delta k_x}{2gh}|\tilde{F}|\cos(\psi_c) + \frac{\mathrm{i}\sin(\psi_c)}{gh}\left(\frac{\mathrm{d}F_{xx}}{\mathrm{d}x} + \frac{F_{xx}}{2\Delta k_x}\frac{\mathrm{d}\Delta k_x}{\mathrm{d}x} + \frac{\Delta k_y}{\Delta k_x}\frac{\mathrm{d}F_{xy}}{\mathrm{d}x}\right)$$

which is written as:

$$\frac{\mathrm{d}\psi_c}{\mathrm{d}x} = -\frac{\mu\Delta k_x}{2} + \frac{\Delta k_x}{2gh\hat{\eta}_f}|\tilde{F}|\cos(\psi_c) + \frac{1}{gh\hat{\eta}_f}$$
$$\times\left(\frac{\mathrm{d}F_{xx}}{\mathrm{d}x} + \frac{F_{xx}}{2\Delta k_x}\frac{\mathrm{d}\Delta k_x}{\mathrm{d}x} + \frac{\Delta k_y}{\Delta k_x}\frac{\mathrm{d}F_{xy}}{\mathrm{d}x}\right)\sin(\psi_c) \tag{C.9}$$

with $\hat{\eta}_f = |T|$ as the WGF IG amplitude. Note that this is a correction of eq. A 23 in Reniers and Zijlema (2022) related to the contribution of $\frac{\Delta k_y^2}{\Delta k_x^2}F_{yy}$ in $\tilde{F}$ to the phase shift evolution. This contribution is expected to be relevant for strongly oblique WGF-IG waves with $\theta_f > 60°$.

Appendix D. Local phase shift expression for obliquely incident bichromatic waves

In the following a expression of the IG phase shift for obliquely incident bichromatic waves is derived for off-resonant conditions. This implies that the resonance mismatch, μ is larger than 1 (see Janssen et al. (2003)). Returning to Eq. (C.1) including the ordering parameter β and the slow spatial scale X given by:

$$-\mu T + \frac{\mathrm{i}\beta}{\Delta k_x}\left(2\frac{\mathrm{d}T}{\mathrm{d}X} + \frac{T}{\Delta k_x}\frac{\mathrm{d}\Delta k_x}{\mathrm{d}X} + \frac{T}{h}\frac{\mathrm{d}h}{\mathrm{d}X}\right) = \tag{D.1}$$

$$\frac{-1}{\rho}\left(-\frac{\hat{S}_{xx}}{gh} - \frac{2\Delta k_y \hat{S}_{xy}}{gh\Delta k_x} - \frac{\Delta k_y^2 \hat{S}_{yy}}{gh\Delta k_x^2} + \frac{\mathrm{i}\beta}{\Delta k_x}\left(\frac{2}{gh}\frac{\mathrm{d}\hat{S}_{xx}}{\mathrm{d}X} + \frac{\hat{S}_{xx}}{gh\Delta k_x}\right.\right.$$
$$\left.\left.\times\ \frac{\mathrm{d}\Delta k_x}{\mathrm{d}X} + \frac{2\Delta k_y}{gh\Delta k_x}\frac{\mathrm{d}\hat{S}_{xy}}{\mathrm{d}X}\right)\right) + O(\beta^2)$$

Assuming that the cross-shore structure of the WGF IG response can be written as a combination of a zeroth order and first order contribution:

$$T = T^{(0)} + T^{(1)} + O(\beta^2) \tag{D.2}$$

collecting the zeroth order contributions yields the classical bound IG wave for a horizontal bed where the forcing and the response are 180 degrees out of phase (Longuet-Higgins and Stewart, 1964):

$$T^{(0)} = \frac{1}{\mu\rho}\left(-\frac{\hat{S}_{xx}}{gh} - \frac{2\Delta k_y \hat{S}_{xy}}{gh\Delta k_x} - \frac{\Delta k_y^2 \hat{S}_{yy}}{gh\Delta k_x^2}\right) = \frac{\tilde{F}}{\mu gh} \tag{D.3}$$

Up to first order in β, using the zeroth order solution for T_0, the following is obtained dropping the ordering parameter β and returning to physical variables:

$$-\mu T^{(0)} - \mu T^{(1)} + \frac{\mathrm{i}}{\Delta k_x}\left(2\frac{\mathrm{d}T^{(0)}}{\mathrm{d}x} + \frac{T^{(0)}}{\Delta k_x}\frac{\mathrm{d}\Delta k_x}{\mathrm{d}x} + \frac{T^{(0)}}{h}\frac{\mathrm{d}h}{\mathrm{d}x}\right) = \tag{D.4}$$

$$\frac{\mathrm{i}}{gh\Delta k_x}\left(2\frac{\mathrm{d}F_{xx}}{\mathrm{d}x} + \frac{F_{xx}}{\Delta k_x}\frac{\mathrm{d}\Delta k_x}{\mathrm{d}x} + \frac{2\Delta k_y}{\Delta k_x}\frac{\mathrm{d}F_{xy}}{\mathrm{d}x}\right) - \frac{\tilde{F}}{gh}$$

Using the zeroth order expression for the IG surface elevation, $T^{(0)}$, the expressions within the first parentheses can be evaluated. Starting with the first term:

$$\frac{\mathrm{i}}{\Delta k_x}\left(2\frac{\mathrm{d}T^{(0)}}{\mathrm{d}x} + \frac{T^{(0)}}{\Delta k_x}\frac{\mathrm{d}\Delta k_x}{\mathrm{d}x} + \frac{T^{(0)}}{h}\frac{\mathrm{d}h}{\mathrm{d}x}\right) = \tag{D.5}$$

$$\frac{\mathrm{i}}{\Delta k_x}\left(\frac{2}{\mu gh}\frac{\mathrm{d}\tilde{F}}{\mathrm{d}x} - \frac{2\tilde{F}}{\mu gh^2}\frac{\mathrm{d}h}{\mathrm{d}x} - \frac{2\tilde{F}}{\mu^2 gh}\frac{\mathrm{d}\mu}{\mathrm{d}x} + \frac{\tilde{F}}{\mu gh\Delta k_x}\frac{\mathrm{d}\Delta k_x}{\mathrm{d}x} + \frac{\tilde{F}}{\mu gh^2}\frac{\mathrm{d}h}{\mathrm{d}x}\right) =$$
$$\frac{\mathrm{i}\tilde{F}}{\mu gh\Delta k_x}\left(\frac{2}{\tilde{F}}\frac{\mathrm{d}\tilde{F}}{\mathrm{d}x} - \frac{1}{h}\frac{\mathrm{d}h}{\mathrm{d}x} - \frac{2}{\mu}\frac{\mathrm{d}\mu}{\mathrm{d}x} + \frac{1}{\Delta k_x}\frac{\mathrm{d}\Delta k_x}{\mathrm{d}x}\right)$$

Collecting all the contributions:

$$-\mu T^{(0)} - \mu T^{(1)} = \tag{D.6}$$

$$\frac{-\mathrm{i}\tilde{F}}{\mu gh\Delta k_x}\left(\frac{2}{\tilde{F}}\frac{\mathrm{d}\tilde{F}}{\mathrm{d}x} - \frac{1}{h}\frac{\mathrm{d}h}{\mathrm{d}x} - \frac{2}{\mu}\frac{\mathrm{d}\mu}{\mathrm{d}x} + \frac{1}{\Delta k_x}\frac{\mathrm{d}\Delta k_x}{\mathrm{d}x}\right) + \frac{\mathrm{i}\tilde{F}}{\mu gh\Delta k_x}$$
$$\times\left(\frac{2\mu}{\tilde{F}}\frac{\mathrm{d}F_{xx}}{\mathrm{d}x} + \frac{\mu}{\tilde{F}}\frac{F_{xx}}{\Delta k_x}\frac{\mathrm{d}\Delta k_x}{\mathrm{d}x} + \frac{\mu}{\tilde{F}}\frac{2\Delta k_y}{\Delta k_x}\frac{\mathrm{d}F_{xy}}{\mathrm{d}x}\right) - \frac{\tilde{F}}{gh}$$

This is rewritten as:

$$T = \frac{\tilde{F}}{\mu gh}\left(1 + \frac{\mathrm{i}}{\mu\Delta k_x}\left(\frac{2}{\tilde{F}}\frac{\mathrm{d}\tilde{F}}{\mathrm{d}x} - \frac{1}{h}\frac{\mathrm{d}h}{\mathrm{d}x} - \frac{2}{\mu}\frac{\mathrm{d}\mu}{\mathrm{d}x} + \frac{1}{\Delta k_x}\frac{\mathrm{d}\Delta k_x}{\mathrm{d}x} - \frac{2\mu}{\tilde{F}}\frac{\mathrm{d}F_{xx}}{\mathrm{d}x}\right.\right.$$

Table E.1
Test case, amplitude, frequency and direction of the two harmonics making up the bichromatic wave indicated by the subscript, m represents the bed slope, $SCI_{\hat{\eta}}$ and SCI_{ψ} are the scatter indices for the WGF-IG amplitude and phase lag differences between the coupled model and the local phase shift predictions. The test-averaged SCI values are 0.37 and 2.88 respectively.

Test	a_1 (m)	a_2 (m)	f_1 (Hz)	f_2 (Hz)	θ_1 (°)	θ_2 (°)	m	$SCI_{\hat{\eta}}$	SCI_{ψ}
B_{01}	0.4	0.1	0.080	0.120	0	15	0.01	0.32	3.19
S_{01}	0.4	0.1	0.080	0.120	0	15	0.04	0.33	3.34
S_{02}	0.4	0.1	0.080	0.120	0	15	0.025	0.33	3.19
S_{03}	0.4	0.1	0.080	0.120	0	15	0.01	0.32	2.47
S_{04}	0.4	0.1	0.080	0.120	0	15	0.005	0.43	2.10
F_{01}	0.4	0.1	0.095	0.105	0	15	0.01	0.77	0.77
F_{02}	0.4	0.1	0.090	0.110	0	15	0.01	0.44	1.82
F_{03}	0.4	0.1	0.085	0.115	0	15	0.01	0.34	2.29
F_{04}	0.4	0.1	0.080	0.120	0	15	0.01	0.32	2.47
T_{01}	0.4	0.1	0.060	0.100	0	15	0.01	0.29	2.98
T_{02}	0.4	0.1	0.098	0.137	0	15	0.01	0.37	2.20
T_{03}	0.4	0.1	0.085	0.115	0	15	0.01	0.32	2.48
T_{04}	0.4	0.1	0.123	0.163	0	15	0.01	0.39	1.88
D_{01}	0.4	0.1	0.080	0.120	0	0	0.01	0.39	3.67
D_{02}	0.4	0.1	0.080	0.120	0	10	0.01	0.30	2.95
D_{03}	0.4	0.1	0.080	0.120	0	20	0.01	0.42	2.09
D_{04}	0.4	0.1	0.080	0.120	0	30	0.01	0.60	1.54
H_{01}	2.0	0.1	0.080	0.120	0	15	0.01	0.13	10.64
H_{02}	1.0	0.1	0.080	0.120	0	15	0.01	0.36	3.80
H_{03}	0.4	0.1	0.080	0.120	0	15	0.01	0.32	2.47
H_{04}	0.2	0.1	0.080	0.120	0	15	0.01	0.29	2.46

$$- \frac{\mu}{\tilde{F}} \frac{F_{xx}}{\Delta k_x} \frac{\mathrm{d}\Delta k_x}{\mathrm{d}x} - \frac{\mu}{\tilde{F}} \frac{2\Delta k_y}{\Delta k_x} \frac{\mathrm{d}F_{xy}}{\mathrm{d}x} \Bigg) \Bigg) \tag{D.7}$$

at $O(\beta)$ this can be written as function of the phase shift:

$$T = \frac{\tilde{F}}{\mu g h} \exp(\mathrm{i}\psi_l) \tag{D.8}$$

where the phase shift is given by:

$$\psi_l = \arg\left(\frac{T}{F}\right) \tag{D.9}$$

corresponding to:

$$\psi_l = \frac{1}{\mu \Delta k_x} \left(\frac{2}{\tilde{F}} \frac{\mathrm{d}\tilde{F}}{\mathrm{d}x} - \frac{1}{h} \frac{\mathrm{d}h}{\mathrm{d}x} - \frac{2}{\mu} \frac{\mathrm{d}\mu}{\mathrm{d}x} + \frac{1}{\Delta k_x} \frac{\mathrm{d}\Delta k_x}{\mathrm{d}x} - \frac{2\mu}{\tilde{F}} \frac{\mathrm{d}F_{xx}}{\mathrm{d}x} - \frac{\mu}{\tilde{F}} \frac{F_{xx}}{\Delta k_x} \frac{\mathrm{d}\Delta k_x}{\mathrm{d}x} - \frac{2\mu}{\tilde{F}} \frac{\Delta k_y}{\Delta k_x} \frac{\mathrm{d}F_{xy}}{\mathrm{d}x} \right) \tag{D.10}$$

These equations show that the phase shift will deviate from zero on a sloping bed as F, Δk_x and μ will change with changes in depth h through the dispersion relation and refraction.

Appendix E. Bichromatic test conditions

An overview of the bichromatic test cases and corresponding error metrics for the phase shift inter comparison are given in Table E.1 below. Test B refers to the base case. Tests S,F,T,D and H refer to the tests where the bed slope, difference frequency, mean wave period, direction and mean wave height have been varied with respect to the base case. Note that tests S_{03}, F_{04} and H_{03} are identical to the base case, but included in the table for easy referencing in the text and Figures.

Appendix F. Coast3D validation error metrics

In the Tables below SCI_c and SCI_l are the scatter indices using the coupled model phase shift and local phase shift respectively. The concurrent bias and root mean square error is given by b_c, b_l, ϵ_c and ϵ_l respectively. The corresponding equations are given by Eqs. (19)–(21).

Table F.1
Error metrics for the prediction of the sea-swell wave height, H_{ss}.

Instrument	$SCI_{H_{ss}}$	$b_{H_{ss}}$ (m)	$\epsilon_{H_{ss}}$ (m)
7a	0.15	−0.05	0.21
7b	0.26	0.19	0.20
1a	0.12	−0.08	0.13
1b	0.12	−0.04	0.12
1c	0.13	0.05	0.09
1d	0.15	0.06	0.10
All	0.15	0.02	0.14

Table F.2
Error metrics for the prediction of the total IG wave height, $H_{ig,t}$ using the coupled model (subscript c) or local phase shift (subscript l).

Instrument	SCI_c	SCI_l	b_c (m)	b_l (m)	ϵ_c (m)	ϵ_l (m)
7a	0.38	0.40	−0.05	−0.05	0.07	0.07
7b	0.14	0.15	−0.02	0.00	0.04	0.03
1a	0.24	0.18	−0.02	−0.01	0.04	0.03
1b	0.29	0.19	−0.04	−0.02	0.06	0.04
1c	0.27	0.18	−0.02	0.01	0.05	0.03
1d	0.26	0.21	0.00	0.01	0.04	0.03
All	0.27	0.22	−0.03	−0.01	0.05	0.04

Table F.3
Error metrics for the prediction of the incoming IG wave height, $H_{ig,i}$ using the coupled model (subscript c) or local phase shift (subscript l).

Instrument	SCI_c	SCI_l	b_c (m)	b_l (m)	ϵ_c (m)	ϵ_l (m)
1a	0.24	0.19	−0.02	−0.01	0.04	0.03
1b	0.31	0.19	−0.04	−0.02	0.05	0.03
1c	0.25	0.15	−0.03	−0.01	0.05	0.03
1d	0.21	0.16	−0.00	0.01	0.03	0.02
All	0.25	0.17	−0.03	−0.01	0.04	0.03

Table F.4
Error metrics for the prediction of the outgoing IG wave height, $H_{ig,o}$ using the coupled model (subscript c) or local phase shift (subscript l).

Instrument	SCI_c	SCI_l	b_c (m)	b_l (m)	ϵ_c (m)	ϵ_l (m)
1a	0.33	0.27	0.00	0.00	0.03	0.02
1b	0.32	0.27	−0.01	−0.00	0.03	0.03
1c	0.31	0.26	−0.01	−0.01	0.04	0.03
1d	0.39	0.36	0.00	0.00	0.03	0.03
All	0.34	0.29	−0.00	−0.00	0.03	0.03

Table F.5
Error metrics for the prediction of the incoming IG wave height at frequency bins 0.01–0.04 Hz at sensor **1a** using the coupled model (subscript c) or local phase shift (subscript l).

IG bin (Hz)	SCI_c	SCI_l	b_c (m)	b_l (m)	ϵ_c (m)	ϵ_l (m)
0.01	0.32	0.29	−0.02	−0.02	0.03	0.02
0.02	0.38	0.33	−0.03	−0.02	0.04	0.03
0.03	0.31	0.23	−0.01	−0.01	0.03	0.02
0.04	0.41	0.32	−0.02	−0.01	0.03	0.03

Table F.6
Error metrics for the prediction of the outgoing IG wave height at frequency bins 0.01–0.04 Hz at sensor **1a** using the coupled model (subscript c) or local phase shift (subscript l).

IG bin (Hz)	SCI_c	SCI_l	b_c (m)	b_l (m)	ϵ_c (m)	ϵ_l (m)
0.01	0.33	0.29	−0.01	−0.01	0.02	0.02
0.02	0.38	0.31	−0.01	−0.00	0.02	0.02
0.03	0.61	0.49	−0.00	−0.00	0.02	0.02
0.04	0.39	0.38	−0.00	−0.00	0.01	0.01

Table F.7
Error metrics at sensor **1a** for the mean incoming IG period, mean outgoing IG period, mean incoming IG direction and mean outgoing IG direction using the coupled model (subscript c) or local phase shift (subscript l).

Par	SCI_c	SCI_l	b_c	b_l	ϵ_c	ϵ_l
$T_{ig,i}$	0.10	0.09	−1.50 (s)	−2.25 (s)	3.68 (s)	3.77 (s)
$T_{ig,o}$	0.13	0.09	0.90 (s)	0.68 (s)	6.31 (s)	4.37 (s)
$D_{ig,i}$	0.65	0.79	−10.7 (°)	−13.5 (°)	11.7 (°)	14.1 (°)
$D_{ig,o}$	0.09	0.06	12.1 (°)	7.8 (°)	15.4 (°)	11.0 (°)

Data availability

Data will be made available on request.

References

Akrish, G., Reniers, A., Rijnsdorp, D., Zijlema, M., Rutten, J., Tissier, M., 2025. The importance of free infragravity waves in the North Sea: Insights from field observations and unstructured SWAN modelling. Ocean. Model. 198, 102619.

Ardhuin, F., Rawat, A., Aucan, J., 2014. A numerical model for free infragravity waves: Definition and validation at regional and global scales. Ocean. Model. 77, 20–32.

Baldock, T.E., 2012. Dissipation of incident forced long waves in the surf zone—Implications for the concept of "bound" wave release at short wave breaking. Coast. Eng. 60, 276–285.

Battjes, J.A., Janssen, J.P.F.M., 1978. Energy loss and set-up due to breaking of random waves. In: Coastal Engineering 1978. American Society of Civil Engineers, pp. 569–587.

Bertin, X., De Bakker, A., Van Dongeren, A., Coco, G., André, G., Ardhuin, F., et al., 2018. Infragravity waves: From driving mechanisms to impacts. Earth-Sci. Rev. 177, 774–799.

Booij, N., Ris, R.C., Holthuijsen, L.H., 1999. A third-generation wave model for coastal regions: 1. model description and validation. J. Geophys. Res. Oceans 104 (C4), 7649–7666.

Bromirski, P.D., Sergienko, O.V., MacAyeal, D.R., 2010. Transoceanic infragravity waves impacting Antarctic ice shelves. Geophys. Res. Lett. 37 (2).

Contardo, S., Lowe, R.J., Hanssen, J.E., Rijnsdorp, D.P., Dufois, F., Symonds, G., 2021. Free and forced components of shoaling long waves in the absence of short-wave breaking. J. Phys. Oceanogr. 51 (5), 1465–1487.

De Bakker, A.T.M., Herbers, T.H.C., Smit, P.B., Tissier, M.F.S., Ruessink, B.G., 2015. Nonlinear infragravity–wave interactions on a gently sloping laboratory beach. J. Phys. Oceanogr. 45 (2), 589–605.

van Dongeren, A., Battjes, J., Janssen, T., van Noorloos, J., Steenhauer, K., Steenbergen, G., Reniers, A., 2007. Shoaling and shoreline dissipation of low-frequency waves. J. Geophys. Res.: Ocean. 112 (C2).

Fiedler, J.W., Smit, P.B., Brodie, K.L., McNinch, J., Guza, R.T., 2019. The offshore boundary condition in surf zone modeling. Coast. Eng. 143, 12–20.

Janssen, T.T., Battjes, J.A., van Dongeren, A.R., 2003. Long waves induced by short-wave groups over a sloping bottom. J. Geophys. Res.: Ocean. 108 (C8).

Lange, A.M.Z., Fiedler, J.W., Merrifield, M.A., Guza, R.T., 2002. Free infragravity waves on the inner shelf: Observations and parameterizations at two southern california beaches. J. Geophys. Res.: Ocean. 129 (8), e2023JC020378.

Lashley, C.H., Jonkman, S.N., Van der Meer, J., Bricker, J.D., Vuik, V., 2022. The influence of infragravity waves on the safety of coastal defences: A case study of the Dutch Wadden Sea. Nat. Hazards Earth Syst. Sci. 22, 1–22.

Leijnse, T.W.B., van Ormondt, M., van Dongeren, A., Aerts, J.C.J.H., Muis, S., 2024. Estimating nearshore infragravity wave conditions at large spatial scales. Front. Mar. Sci. 11, 1355095.

Liao, Z., Li, S., Liu, Y., Zou, Q., 2021. An analytical spectral model for infragravity waves over topography in intermediate and shallow water under nonbreaking conditions. J. Phys. Oceanogr. 51 (9).

Liao, Z., Zou, Q., Liu, Y., Contardo, S., Li, S., 2023. Unified analytical solution for group-induced infragravity waves based on green's function. J. Fluid Mech. 967 (A37).

Longuet-Higgins, M.S., Stewart, R.W., 1964. Radiation stress in water waves: a physical discussion with applications. Deep-Sea Res. 529–562.

Lygre, A., Krogstad, H.E., 1986. Maximum entropy estimation of the directional distribution in ocean wave spectra. J. Phys. Oceanogr. 16 (12), 2052–2060.

Ma, G., Su, S.-F., Liu, S., Chu, J.-C., 2014. Numerical simulation of infragravity waves in fringing reefs using a shock-capturing non-hydrostatic mode. Ocean Eng. 85, 54–64.

Matsuba, Y., Roelvink, D., van Dongeren, A., 2024. Propagation of free infragravity waves generated at distant beaches. J. Geophys. Res.: Ocean. 129 (10), e2023JC020580.

Matsuba, Y., Roelvink, D., Reniers, A.J.H.M., Rijnsdorp, D.P., Shimozono, T., 2022. Reconstruction of directional spectra of infragravity waves. J. Geophys. Res.: Ocean. 127 (7), e2021JC018273.

Okihiro, M., Guza, R.T., 1995. Infragravity energy modulation by tides. . Geophys. Res. 100, 16,143–16,148.

Okihiro, M., Guza, R.T., Seymour, R.J., 1993. Excitation of seiche observed in a small harbor. J. Geophys. Res.: Ocean. 98 (C10), 18201–18211.

Olabarrieta, M., Warner, J.C., Hegermiller, C.A., 2023. Development and application of an infragravity wave (InWave) driver to simulate nearshore processes. J. Adv. Model. Earth Syst. 15 (6), e2022MS003205.

Pearson, S.G., Storlazzi, C.D., van Dongeren, A.R., Tissier, M.F.S., Reniers, A.J.H.M., 2017. A Bayesian-based system to assess wave-driven flooding hazards on coral reef-Lined Coasts. J. Geophys. Res.: Ocean. 122 (12), 10099–10117.

Raubenheimer, B., Guza, R.T., 1996. Observations and predictions of run-up. J. Geophys. Res. 101 (C11), 25575–25587.

Reniers, A.J.H.M., van Dongeren, A.R., Battjes, J.A., Thornton, E.B., 2002. Linear modeling of infragravity waves during delilah. J. Geophys. Res.: Ocean. 107 (C10), 3137.

Reniers, A.J.H.M., MacMahan, J.H., Thornton, E.B., Stanton, T.P., 2006. Modelling infragravity motions on a rip-channel beach. Coast. Eng. 53 (2–3), 209–222, cited By (since 1996) 2.

Reniers, A., Zijlema, M., 2022. SWAN SurfBeat 1D. Coast. Eng. 172, 104068.

Reyns, J., McCall, R., Ranasinghe, R., van Dongeren, A., Roelvink, D., 2023. Modelling wave group-scale hydrodynamics on orthogonal unstructured meshes. Environ. Model. Softw. 162, 105655.

van Rijn, L.C., Walstra, D.J.R., Grasmeijer, B., Sutherland, J., Pan, S., Sierra, J.P., 2003. The predictability of cross-shore bed evolution of sandy beaches at the time scale of storms and seasons using process-based profile models. Coast. Eng. 47, 295–327.

Rijnsdorp, D.P., Reniers, A.J.H.M., Zijlema, M., 2021. Free infragravity waves in the North Sea. J. Geophys. Res.: Ocean. 126, e2021JC017368.

Rijnsdorp, D.P., Ruessink, B.G., Zijlema, M., 2015. Infragravity-wave dynamics in a barred coastal region, a numerical study. J. Geophys. Res.: Ocean. 120 (6), 4068–4089.

Rijnsdorp, D.P., Wolgamot, H., Zijlema, M., 2022. Non-hydrostatic modelling of the wave-induced response of moored floating structures in coastal waters. Coast. Eng. 177, 104195.

Roeber, V., Bricker, J.D., 2015. Destructive tsunami-like wave generated by surf beat over a coral reef during Typhoon Haiyan. Nat. Commun. 6 (8854).

Roelvink, D., Reniers, A., Van Dongeren, A., De Vries, J.V.T., McCall, R., Lescinski, J., 2009. Modelling storm impacts on beaches, dunes and barrier islands. Coast. Eng. 56 (11–12), 1133–1152.

Ruessink, B.G., 1998. Bound and free infragravity waves in the nearshore zone under breaking and nonbreaking conditions. J. Geophys. Res.: Ocean. 103 (C6), 12795–12805.

Ruessink, B.G., 1999. COAST 3D: Data Report 2.5D Experiment Egmond Aan Zee. Technical Report EC MAST Project No. MAS3-CT97-0086. Technical report, IMAU, Utrecht University.

Ruessink, B.G., Miles, J.R., Feddersen, F., Guza, R.T., Elgar, S., 2001. Modeling the alongshore current on barred beaches. J. Geophys. Res.: Ocean. 106 (C10), 22451–22463.

Schäffer, H.A., 1993. Infragravity waves induced by short-wave groups. J. Fluid Mech. 247, 551–588.

Smit, P., Janssen, T., Herbers, T., Taira, T., Romanowicz, B., 2018. Infragravity wave radiation across the shelf break. J. Geophys. Res.: Ocean. 123 (7), 4483–4490.

Smit, P., Janssen, T., Holthuijsen, L., Smith, J., 2014. Non-hydrostatic modeling of surf zone wave dynamics. Coast. Eng. 83, 36–48.

Soulsby, R.L., 1999. Coastal sediment transport: the COAST 3D project. In: Coastal Engineering 1998. American Society Of Civil Engineers, pp. 2548–2558.

Symonds, G., Huntley, D.A., Bowen, A.J., 1982. Two-dimensional surf beat: Long wave generation by a time-varying breakpoint. J. Geophys. Res.: Ocean. 87, 492–498.

Thomson, J., Elgar, S., Raubenheimer, B., Herbers, T.H.C., Guza, R.T., 2006. Tidal modulation of infragravity waves via nonlinear energy losses in the surfzone. Geophys. Res. Lett. 33.

Van Dongeren, A., Reniers, A.J.H.M., Battjes, J.A., Svendsen, I., 2003. Numerical modeling of infragravity wave response during DELILAH. J. Geophys. Res.: Ocean. 108 (C9).

van Wiechen, P.P.J., de Vries, S., Reniers, A.J.H.M., Aarninkhof, S.G.J., 2023. Dune erosion during storm surges: A review of the observations, physics and modelling of the collision regime. Coast. Eng. 186, 104383.

Zhang, Q., Toorman, E.A., Monbaliu, J., 2020. Shoaling of bound infragravity waves on plane slopes for bichromatic wave conditions. Coast. Eng. 158, 103684.